LATVIAN
JOURNAL
of
PHYSICS
and TECHNICAL
SCIENCES

ISSN 0868 - 8257

5

(Vol. 57)

2020

CONTENTS

LATVIAN JOURNAL of PHYSICS and TECHNICAL SCIENCES

LATVIJAS FIZIKAS un TEHNISKO ZINĀTŅU ŽURNĀLS

ЛАТВИЙСКИЙ ФИЗИКО-ТЕХНИЧЕСКИЙ ЖУРНАЛ

Published six times a year since February 1964
Iznāk sešas reizes gadā kopš 1964. gada februāra
Выходит шесть раз в год с февраля 1964 года

5 (Vol. 57) • **2020**

RĪGA

Language Editor: O. Ivanova
Computer Designer: I. Begicevs

INDEXED (PUBLISHED) IN

www.scopus.com
www.sciendo.com
EBSCO (Academic Search Complete, www.epnet.com), INSPEC (www.iee.org.com).
VINITI (www.viniti.ru), Begell House Inc/ (EDC, www.edata-center.com).

Issuers: Institute of Physical Energetics,
Institute of Solid State Physics, University of Latvia
Registration Certificate Number: 000700221

Editorial Contacts:
11 Krivu Street, Riga, LV - 1006
Ph.: + 371 67551732
E-mail: leo@lza.lv
www.fei-web.lv

IN MEMORIAM

Full Member of the Estonian Academy of Sciences

Cheslav Lushchik

(15.02.1928–08.08.2020)

Cheslav Lushchik, one of the world leaders in radiation physics of ionic crystals, died on 8 August 2020 at the age of 92 in Tartu, Estonia. He has discovered that excitation of electrons and excitons in ionic crystals leads to the creation of lattice defects and luminescence and how it is responsible for radiation damage of these materials under different types of irradiation. Being one of the most outstanding solid state physicists of his generation, he co-authored three monographs and more than 400 publications and his numerous former colleagues, undergraduate and postgraduate students contribute to research in various countries.

Cheslav Lushchik was born in 1928 in St. Petersburg. At the age of thirteen, he survived the blockade of Leningrad, where his mother died. In 1951, he graduated with honours from Leningrad University and, in 1954, defended the Doctoral Thesis on crystal thermal activation spectroscopy. In the same year, he was invited by his scientific supervisor, Professor Feodor Klement, to work at Tartu State University, to which he devoted his entire life.

In 1954, Cheslav Lushchik became a senior researcher at the Estonian Institute of Physics and Astronomy in Tartu. In 1964, he defended the Doctoral Thesis at the Leningrad Institute of Optics and in the same year was elected the full member of the Estonian Academy of Sciences. From 1960, he held various positions at the Institute of Physics and Astronomy and was the Head of the Luminescence Laboratory and the Ionic Crystal Physics Laboratory until 1994.

Professor Lushchik founded and led the Scientific School of Insulating Crystal Physics in Tartu and strongly influenced the development of this research field in the former USSR and internationally. His ideas inspired several generations of researchers in Estonia and more widely with more than 50 Doctoral Theses completed and defended under his supervision by PhD students from Latvia, Russia, Kazakhstan, and Kyrgyzstan.

Professor Lushchik made great contribution to the development of solid state and radiation physics in Latvia. Since the 1960s, some of the first Latvian PhD students in solid state physics have been trained at Tartu State University. The development of solid state physics in Latvia was also facilitated by his lectures on physics of ionic crystals at the Faculty of Physics and Mathematics of the Latvia State University.

He was one of the organisers of the Baltic workshops/seminars on Physics of Ionic Crystals, which started in 1967 on his suggestion, and played a special role in the development of solid state and radiation physics and chemistry in the former USSR. They took place twice per year, until 1991, in Riga and Tartu, bringing together physicists from all over the Soviet Union and served as a hotbed of new ideas.

Creative collaboration with Cheslav Lushchik promoted research in the field of solid state physics at the Institute of Physics of the Latvian Academy of Sciences, and his ideas inspired the activities of the Institute of Solid State Physics of the University of Latvia during its establishment and development.

Cheslav Lushchik dedicated all his life and carrier to scientific research and will be widely remembered by his former colleagues and students as an outstanding researcher of great integrity and commitment.

Roberts Evarestov,
Eugene Kotomin,
Anatoli Popov,
Kurt Schwartz,
Alex Shluger.

LATVIAN JOURNAL OF PHYSICS
AND TECHNICAL SCIENCES
2020, N 5

DOI: 10.2478/lpts-2020-0023

COMPUTER SIMULATION TO OPTIMIZE THE VFA ALPHA PROTOTYPE WITH A HYDRAULIC PISTON COMPRESSOR AND AN INTEGRATED BOOSTER

A. Mezulis[1]*, A. Safronov[2], J. Guzeyeva[2], J. Begens[2]
[1]Institute of Solid State Physics, University of Latvia, 8 Kengaraga Str., Riga, LV-1063, LATVIA
[2]Hygen Ltd., 7 Peldu Str., Jelgava, LV-3002, LATVIA
*e-mail: ansis.mezulis@cfi.lu.lv

Natural gas, including biomethane, is a sustainable alternative fuel. Widening compressed natural gas applications by now is restricted by weakly developed infrastructure. Hygen Ltd. works on “hydraulic piston” technology for natural gas and biomethane compressing, storing, delivering and discharging the storage cylinders by means of an innovative hydraulic boosting technology. Designing of the Vehicle Fuelling Appliance (VFA) demands to take into account thermodynamics and gas dynamics properties at fluid compression and motion. The present paper deals with theoretical characteristics and their link to test measurements regarding a particular VFA HYGEN+ Alpha prototype manufactured by Hygen Ltd.

Keywords: *Gas compression, gas refuelling, gas storage, gas thermodynamics, Matlab simulation, reservoir engineering and simulation.*

1. INTRODUCTION

Nowadays the alternative fuels are defined by the Directive of the European Parliament and of the Council on the deployment of alternative fuel infrastructure (DAFI). One of them is natural gas (NG), including biomethane – the upgraded biogas, which is considered the renewable fuel with close to zero greenhouse gas emissions in Well-to-Wheel scale. DAFI sets out minimum requirements for the building-up of alternative fuel infrastructure, including refuelling points to be implemented by means of Member States’ national policy frameworks [1]. On 21 January 2020, the European Biogas Association (EBA), the Natural & bio Gas Vehicle Association (NGVA Europe) and the European Automobile Manufacturers’ Association (ACEA) called on the EU policy makers to accelerate the deployment of infrastructure to deliver natural gas and renewable gas/biomethane across the European Union [2].

Technical problems of widening the compressed natural gas (CNG) and bio-gas (bio-CNG) application under off-grid conditions are as follows:

- storage cylinder filling to high pressure in an efficient and cost-effective way;
- CNG/bio-CNG delivery to the destination (injection point to the grid or fuelling station);
- development of an efficient fuelling appliance;
- complete gas storage cylinder dischargement.

To solve these technical problems, in 2008 Latvian engineer Aleksey Safronov invented and patented a new method for hydraulic compression of gaseous fuels and a device for implementation thereof [3]. A manufacturer from Latvia Hygen Ltd. [4] has developed a "hydraulic piston" technology intended for gas compression, accumulation and discharge, and implemented it in various CNG fuelling systems. Unlike conventional mechanical multistage compressors, the technology of hydraulic piston uses a method of gas compression by means of a working fluid, which is pushed by a sufficiently powerful hydraulic pump. The technology of hydraulic compression allows building autonomous modules to be placed on the mobile carrier.

Technical innovation of the "hydraulic piston" technology described in the present paper is the boosting stage that accomplishes gas fuelling after the free flow stage up to reaching the nominal pressure in the receiver cylinder. Developed to the vehicle fuelling appliance level, the hydraulic compressor module with a boosting regime solves the technical problems stated above in small and even medium amount of the demanded gas supply.

2. EXPERIMENTAL: WORKING STAGES OF THE HYDRAULIC COMPRESSOR

2.1. COMPRESSION AND GAS STORAGE STAGE

Technology of hydraulic piston compression and compressed gas storage in a cylinder is explained in Fig. 1.

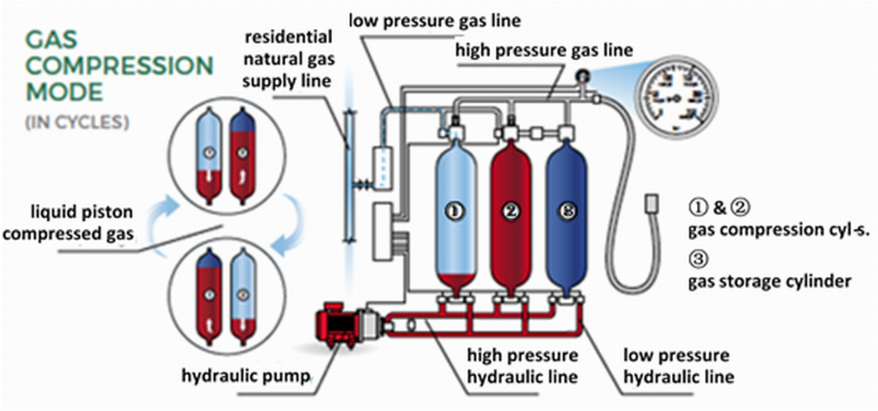

Fig. 1. Hydraulic piston compressor and storage.

Cylinders 1 and 2 work as compressors. The amount of the working liquid (red fill in Fig. 1) slightly exceeds the volume in one compression cylinder. The working liquid is chosen to avoid any chemical reaction with the gas, as well as have minimized gas diffusivity. Typical working liquid for a gas piston is transmission oil. By rotating the hydraulic pump and triggering the valves, the working liquid is alternatively pumped between the first and second compression cylinders. Increasing the amount of liquid in a compressor cylinder causes compression of low-pressure gas above the liquid. At the same time, a decrease of liquid in another compression cylinder makes use for inlet of a new portion of low-pressure gas. In the present Alpha prototype volume free of liquid is 26 L, productivity of the hydraulic pump is 8.64 L/min, and the resulting compression step is 3 minutes long. Inlet gas pressure can vary in wide range, starting from residential low pressure of 17–25 mbar up to industrial high pressures. Too low gas inlet pressure considerably reduces the efficiency of compressing; therefore, for low pressure a pre-compression up to 3 bars is accomplished. At the end phase of each compression cycle, when gas pressure in the compression cylinder surpasses that in the storage cylinder, a current portion of gas is pushed through the check valve into the storage cylinder. As a result of compression in multiple cycles, storage cylinder 3 is filled up with the gas, up to 200 bars. Driving all hydraulic and gas valves is implemented by the electronic control unit.

Computer simulation of the compression stage is useful not only to see the number of compression cycles to fill the storage cylinder, but also to see thermal characteristics. Note that the average outlet temperature of the gas must not reach the safety threshold of any type of a standard fuel tank, starting from 60 °C.

For the simulation, we use Matlab Simscape elements with their mathematical description (Ref. [5] for Subsections 2.1 and 2.2). For the storage cylinder a constant volume chamber is chosen. The enclosure of this element can exchange mass and energy with the connected gas network, as well as exchange heat with the environment, allowing its internal pressure and temperature to evolve over time. Mass *M* conservation relates the mass flow rate $\dot{m}_A$ to the dynamics of the pressure *p* and temperature *T* of the internal node *I*, representing the gas volume

$$\frac{\partial M}{\partial p}\cdot\frac{dp_I}{dt}+\frac{\partial M}{\partial T}\cdot\frac{dT_I}{dt}=\dot{m}_A. \tag{1}$$

Energy *U* conservation relates the energy $\dot{\Phi}_A$ and heat flow $\dot{Q}_H$ rates to the dynamics of the pressure and temperature of the internal node, representing the gas volume

$$\frac{\partial U}{\partial p}\cdot\frac{dp_I}{dt}+\frac{\partial U}{\partial T}\cdot\frac{dT_I}{dt}=\dot{\Phi}_A+\dot{Q}_H. \tag{2}$$

As the gas enters the storage cylinder by small portions every 3 minutes, the overall temperature within the cylinder has enough time to equilibrate. Consequently, no convective heat exchange is considered, and the cylinder body can be represented as the thermal mass

$$\dot{Q}_H = c m_{cyl}\frac{dT}{dt}, \tag{3}$$

where *c* is specific heat capacity of material of the cylinder. The outer surface of the cylinder is in convective thermal contact with the ambient air.

Each compression cylinder represents the translational volume *V* converter. The mass and energy conversation equations are similar to those of a constant volume chamber, except for an additional term in each equation

$$\frac{\partial M}{\partial p}\cdot\frac{dp_{\mathrm{I}}}{dt}+\frac{\partial M}{\partial T}\cdot\frac{dT_{\mathrm{I}}}{dt}+\rho_{\mathrm{I}}\frac{dV}{dt}=\dot{m}_A, \tag{4}$$

$$\frac{\partial U}{\partial p}\cdot\frac{dp_{\mathrm{I}}}{dt}+\frac{\partial U}{\partial T}\cdot\frac{dT_{\mathrm{I}}}{dt}+\rho_{\mathrm{I}}h_{\mathrm{I}}\frac{dV}{dt}=\dot{\Phi}_A+\dot{Q}_H, \tag{5}$$

where ρ and h are density and specific enthalpy of the internal node *I*. A correct description of heat exchange between compressed gas and thermal bodies in the compression cylinder is very complicated. Increase in the amount of the working liquid in the cylinder increases its thermal mass; on the other hand, this process decreases the area of cylinder body that is in contact with the compressed gas. Additionally, at the temperature above 100–200 °C the energy loss due to thermal radiation is not negligible. Such a complicated model is not the aim of the present study. We restrict our theoretical model by creating a link between it and test experiment data, which helps evaluate the main characteristics of the fans, which are necessary for cooling the heads of compressor cylinders. Thermal parameters of the gas pipeline play a minor role because at the compression stage gas is transmitted via pipeline by small discrete portions.

2.2. FREE FLOW STAGE

By filling a target tank of initial pressure lower than 200 bars, the first filling stage is free flow stage. This stage lasts until pressure equilibrium between the storage tank and the target tank is achieved.

The pipeline, in which viscous friction forces act, as well as local restrictions have to be taken into account carefully. The Alpha prototype device has M8x1 steel tube of 2 m long, which is connected to 3/8” of 4 m long outer rubber tube in free gas flow circuit. For Matlab simulation, we take a pipe, which accounts for viscous friction losses and convective heat transfer with the pipe wall. The pressure and temperature in the pipe evolve based on the compressibility and thermal capacity of the gas volume. Choking occurs when the outlet reaches the sonic condition. The mass and energy conversation equations are as follows:

$$\frac{\partial M}{\partial p}\cdot\frac{dp_{\mathrm{I}}}{dt}+\frac{\partial M}{\partial T}\cdot\frac{dT_{\mathrm{I}}}{dt}=\dot{m}_A+\dot{m}_B, \tag{6}$$

$$\frac{\partial U}{\partial p}\cdot\frac{dp_{\mathrm{I}}}{dt}+\frac{\partial U}{\partial T}\cdot\frac{dT_{\mathrm{I}}}{dt}=\dot{\Phi}_A+\dot{\Phi}_B+\dot{Q}_H, \tag{7}$$

where *A* denotes inlet, and *B* is an outlet port of the pipe.

The momentum balance for each half from the middle point *I* of the pipe models the pressure drop due to momentum flux and viscous friction

$$p_A-p_{\mathrm{I}}=\left(\frac{\dot{m}_A}{S}\right)^2\cdot\left(\frac{1}{\rho_{\mathrm{I}}}-\frac{1}{\rho_A}\right)+\Delta p_{AI}, \tag{8}$$

$$p_B-p_{\mathrm{I}}=\left(\frac{\dot{m}_B}{S}\right)^2\cdot\left(\frac{1}{\rho_{\mathrm{I}}}-\frac{1}{\rho_B}\right)+\Delta p_{BI}, \tag{9}$$

where Δp_{AI} and Δp_{BI} are pressure losses due to viscous friction, which are distinguished for laminar and turbulent flow, and *S* is the cross-sectional area. The upper Reynolds number of laminar flow *Re* is commonly chosen as 2000, and in the laminar flow regime the pressure losses due to viscous friction are as follows:

$$\begin{aligned}\Delta p_{AI(lam)}&=f_{sh}\frac{\dot{m}_A\cdot\mu_I\cdot L}{4\rho_I\cdot S\cdot D_h^2}\ ;\\ \Delta p_{BI(lam)}&=f_{sh}\frac{\dot{m}_B\cdot\mu_I\cdot L}{4\rho_I\cdot S\cdot D_h^2}\ ,\end{aligned} \tag{10}$$

where f_{sh} – the shape factor for laminar flow viscous friction, μ – dynamic viscosity, *L* – pipe length, D_h – hydraulic diameter. The turbulent flow starts from the lower Reynolds number of turbulent flow, which is usually taken as 4000. For turbulent flow regime

$$\Delta p_{AI(tur)} = f_{Dar}\frac{\dot{m}_A \cdot |\dot{m}_A| \cdot L}{4\rho_I \cdot D_h \cdot S^2} ;$$
$$\Delta p_{BI(tur)} = f_{Dar}\frac{\dot{m}_B \cdot |\dot{m}_B| \cdot L}{4\rho_I \cdot D_h \cdot S^2} . \quad (11)$$

Note that in turbulent flow the laminar shape factor f_{sh} is replaced by the Darcy friction factor f_{Dar}, which is widely computed from the Haaland correlation

$$f_{Dar} = \left[-1.8log\left(\frac{6.9}{Re} + \left(\frac{\varepsilon_r}{3.7D_h}\right)^{1.11}\right)\right]^{-2} . \quad (12)$$

The absolute roughness of internal surface ε_r of different materials can be found in the tables. We take 0.05 mm for a commercial steel tube and 0.002 mm for the liner of the rubber tube.

The flow regime of the Reynolds number 2000–4000 is mixed. The pressure losses due to viscous friction in the mixed regime follow a smooth connection between those in the laminar flow and those in the turbulent flow.

The convective heat transfer equation between the pipe wall and the gas volume is governed by the Newton's law of cooling

$$\dot{Q}_H = \propto_T \frac{4SL}{D_h}(T_H - T_I). \quad (13)$$

The heat transfer coefficient α_T depends on the Nusselt number

$$\propto_T = \left(\frac{Nu_A + Nu_B}{2}\right) \cdot \frac{\lambda}{D_h}, \quad (14)$$

where λ is thermal conductivity of the fluid. The Nusselt numbers Nu_A and Nu_B depend on the flow regime. The Nusselt numbers in the laminar flow regime are constant and equal to the set value, which is usually 3.66. The Nusselt numbers in the turbulent flow regime are computed from the Gnielinski correlation

$$Nu_{(tur)} = \frac{(Re-1000)Pr_I \cdot \frac{f_{Dar}}{8}}{1+1.27 \cdot \left(Pr_i^{1.5}-1\right)\left(\frac{f_{Dar}}{8}\right)^{0.5}}, \quad (15)$$

where Pr is the Prandtl number: $Pr = c_p\mu/\lambda$. The Nusselt numbers in the mixed regime follow a smooth connection between those in the laminar flow and those in the turbulent flow.

In the case of flow choking, the mass flow rates out of the pipe at ports A and B are as follows:

$$\dot{m}_{A(Ch)} = \rho_A v_A S ; \quad \dot{m}_{B(Ch)} = \rho_B v_B S, \quad (16)$$

where v_A, v_B are the speed of sound at ports A and B, respectively.

The choked pressure is obtained by substituting the choked mass flow rate into the momentum balance equations for the pipe. For the port A

$$p_{A(Ch)} = p_I + \left(\frac{\dot{m}_{A(Ch)}}{S}\right)^2 \cdot$$
$$\cdot \left(\frac{1}{\rho_I} - \frac{1}{\rho_A}\right) + \Delta p_{AI(Ch)}. \quad (17)$$

$\Delta p_{A(Ch)}$ is the pressure loss due to viscous friction, assuming that the choking has occurred.

At the free flow stage, gas molecules enter the receiver cylinder at high velocity; therefore, a convective heat exchange (forced convection) between the gas and the cylinder body takes place [6]. In a particular case, the velocity of gas and its direction relative to the cylinder body, as well as other parameters are far from being constant. Since the aim of the present Matlab simulation is to get theoretical characteristics of medium accuracy, the authors evaluate for use the mean value of the convective heat exchange coefficient α_T for a particular setup of 300 W/m^2·K. The heat exchange between outer surfaces of all cylinders and ambient air is considered to be the air free convection with a coefficient of 10 W/m^2·K.

Presence of a significant pressure drop causes acting the Joule-Thomson effect within a non-ideal gas. Numerically, the Joule-Thomson effect is characterised as follows:

$$\mu_{J-T} = \left(\frac{\partial T}{\partial p}\right)_H , \tag{18}$$

where the index H represents a partial derivative at constant enthalpy. The Joule-Thomson effect in natural gas is widely investigated; nevertheless, taking it into account is rather complicated because its value strongly depends on absolute pressure and temperature [7], [8]. As a solution, Matlab simulation allows building multi-dimensional data arrays, in a particular case, $\mu_{J-T}(p,T)$. Since the inlet of the target tank is the only location for a significant pressure drop, we address all temperature drop due to the Joule-Thomson effect to entering gas in the target tank.

2.3. BOOSTING STAGE

In order to empty storage cylinder 3 (Fig. 1) of gas far behind the free flow level, the boosting mode is implemented. The principle of boosting is displayed in Fig. 2.

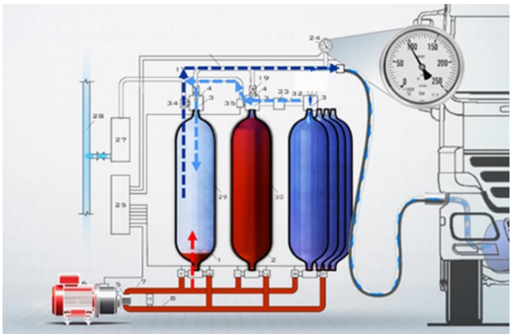

Fig. 2. Hydraulic piston operating in a boosting mode.

When the storage tank is connected to the vehicle receptacle, fuelling occurs by free flow until pressure equilibrium is achieved. After the free flow stage, the remaining mid-pressure gas from the storage cylinder (light blue arrow) is supplied to the compressing cylinder for boosting, where it is further compressed by the hydraulic piston and forced out directly into the vehicle fuel tank (dark blue arrow). Boosting cycles repeat alternately in two compression cylinders. The number of boosting cycles to achieve the pressure of 200 bars in the vehicle fuel tank depends on the volume and initial pressure of the tank. In case of a mid-sized tank of 240 L, about 10 single boosting cycles are enough to fill the vehicle completely. Obviously, if VFA contains two compressors, the number of boosting cycles must be divided by two.

From the mathematical simulation point of view, the boosting stage combines the models of free flow and compression. Choking, turbulent and Joule-Thomson effects at the boosting stage from the storage to the compressor cylinder are not so intense as at the free flow stage because of less initial pressure difference and higher ratio between donor and receiver volumes (190 L vs. 26 L for one compressor cylinder). As the gas inlet pressure is more than ten times higher (30… 120 bars vs. 3 bars), the transferred mass portion from each compression cycle at the boosting stage is significantly larger than that at the compression stage.

3. RESULTS

VFA HYGEN+ Alpha prototype consists of two compressors (four cylinders, 32 L each) and storage volume (four cylinders, 95 L each). One must be careful to simulate the stages regarding only one compression cylinder. At the compression stage, each compression cylinder fills one fourth of storage volume; thus, the storage volume must be taken of 95 L for a correct stored NG mass growth. At the free flow stage, the compressor is not employed, and all storage volume of 380 L must be simulated. The boosting stage is the most complicated case: a half of storage volume fills the compression cylinder of one pair, and, in turn, one compression pair boosts a half of the target tank. Ambient air temperature, as in Northern Europe, is taken 20 °C.

3.1. SIMULATION OF THE GAS COMPRESSION AND STORAGE STAGE

Matlab simulation of the gas compression and storage stage is based on Eqs. (1)–(5), and the obtained main characteristics are shown in Fig. 3. For better resolution only last 120 min of the whole compression is displayed, i.e., from 185 to 205 bars (ending pressure of the compression is adjusted a bit over 200 bars as a correction to following cool-down of receiver cylinders). Stored mass of NG increases in equal steps, as NG inlet amount in the compression cylinder ("donor" in Fig. 3) is constant and not depending on the end pressure. The pressure in the storage cylinder ("receiver" in Fig. 3) also grows in equal steps, as its temperature increases very slightly.

The temperature growth of NG at compressing to gradually higher pressures has to be restricted at the end of process not to reach the safety threshold of any gas cylinder type. As the donor temperature at compressing is higher at the boosting stage, the necessary temperature restriction by means of installing the fans is optimized at a latter stage.

Figures 3c, 3d show that temperature of the gas in the pipeline during the idle time of mass transfer relaxes in a rather wide range.

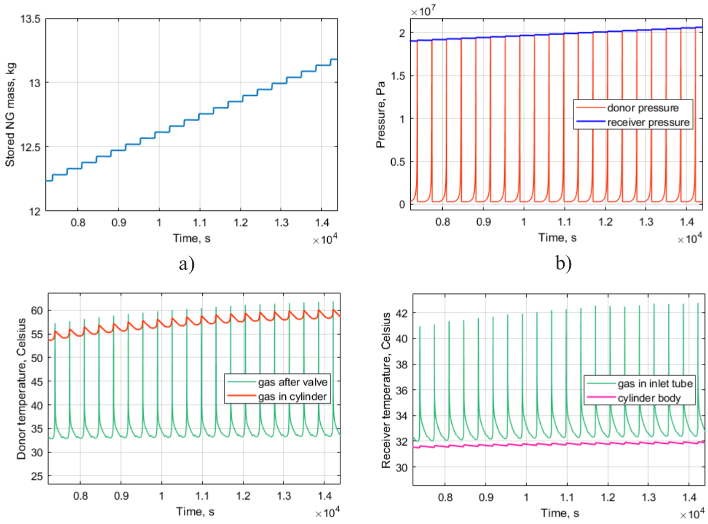

a) b) c) d)

Fig. 3. Matlab simulated physical characteristics of the gas compression and storage stage.

3.2. SIMULATION OF THE FREE FLOW STAGE

Matlab simulation of the free flow stage basically regards Eqs. (6)–(9) with addition of Eqs. (10)–(18). Figure 4 depicts the obtained main characteristics of the free flow stage. The vehicle tank is assumed as mid-sized, 240 L, with the initial pressure of 10 and 80 bars. Figure 4b shows that equilibrium pressure at the end of the free flow stage is ca. 128 and 158 bars, respectively. According to thermodynamics, the temperature of NG in the donor cylinder is rapidly decreasing, whereas in the receiver cylinder increasing during high NG mass flow rate (Figs. 4c, 4d). Very low temperature of NG, entering the receiver cylinder at the initial stage, is caused by acting the Joule-Thomson effect.

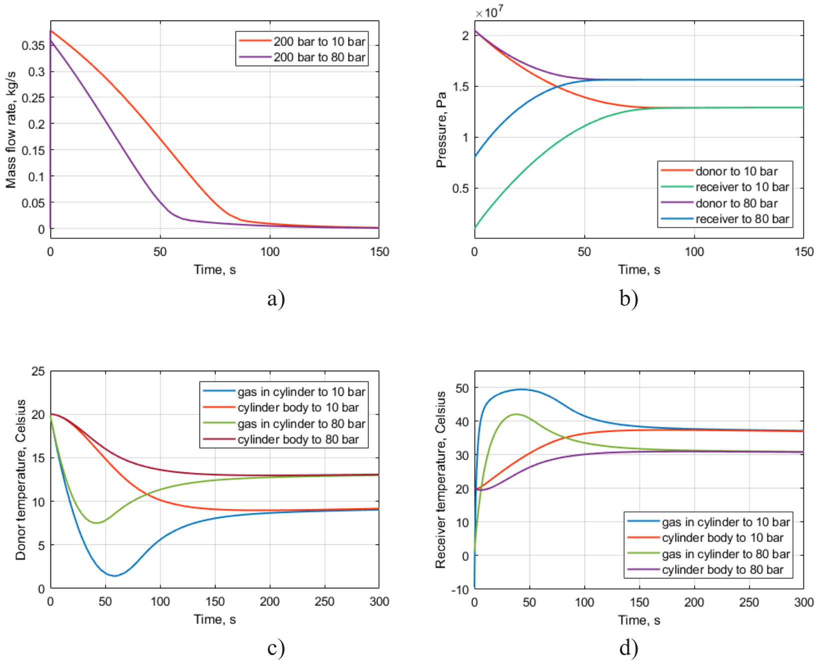

a) b)

c) d)

Fig. 4. Matlab simulated physical characteristics of the free flow stage.

3.3. SIMULATION OF THE BOOSTING STAGE

The boosting stage includes both the free flow and compression stages; therefore, all equations cited above are used in Matlab simulation, Eqs. (1)–(9) with addition of Eqs. (10)–(18). Figure 5 depicts the obtained main characteristics of the boosting stage for the case of 240 L target tank with initial pressure of 10 bars. The whole boosting process, which follows the free flow stage and lasts 30 minutes, is displayed.

Boosted mass of NG increases in descending steps, as NG source is the storage cylinders with restricted volume. The pressure (Fig. 5b) in the target tank increases in descending steps as well, reaching preset 205 bar in 5 boosting steps performed by one compressor cylinder of the pair.

The temperature growth in the compressor ("donor" in Fig. 5c) cylinder is of major interest. As said above, it has to be restricted at the end of process. Matlab simulation without the forced convective air flow around the heads of compressor cylinders returns an overheating by 15–20 °C. We estimate the dissipated power P that results in the heat excess. In the first-order approximation we assume that excess heat dissipates from the surface at the head of compression cylinder, twice its cross-section, 0.075 m^2. Thus, $P=cm\Delta T/\tau=125$ W, where τ is the period of compression cycles, equal to 360 s. Calculators, tables and plots to find necessary parameters of a fan are widely accessible. We use a simple calculator designed by Stego Ltd. [9]. For a device, designed for Northern and Central Europe, we choose maximum ambient temperature as 40 °C and designed interior temperature as 65 °C. With the power dissipation of 125 W, the calculator returns the required volume flow of 15.5 m^3/h that can be ensured by a medium-sized fan. Including the determined cooling parameters in Matlab simulation, as a result, we get average temperature growth from 40 °C to 72 °C approximately (Fig. 5c), which is quite acceptable taking into account that there is the amount of NG at temperature below 40 °C in the target tank after the free flow stage.

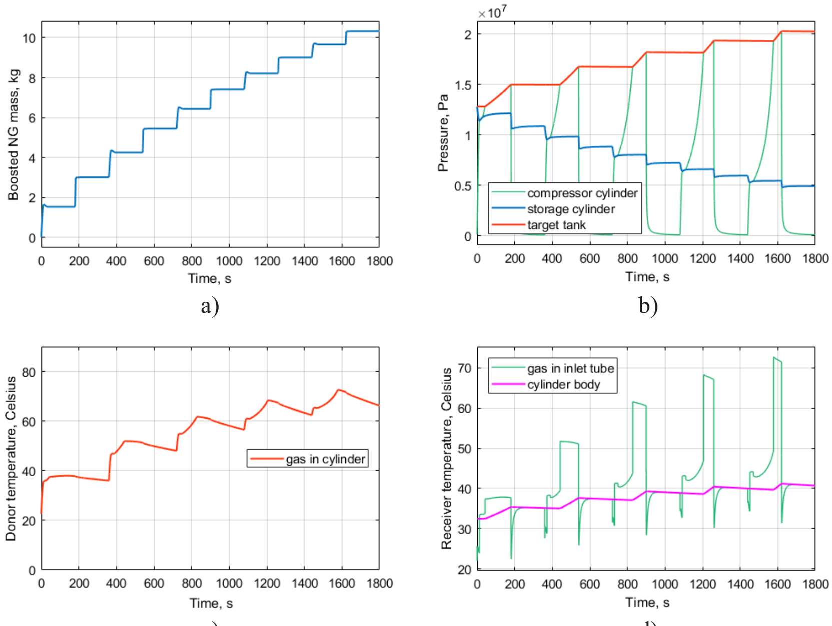

a) b)

c) d)

Fig. 5. Matlab simulated physical characteristics of the boosting stage.

3.4. APPLYING THE RESULTS OF SIMULATION TO HYGEN+ ALPHA PROTOTYPE

To test the HYGEN+ Alpha prototype, we install customary manometers in gas tubing nodes. Installing the pressure measuring sensors of high precision inside the cylinders and gas tubing is a rather complicated task due to maximum pressure of 200 bars and rapid temperature changes. Moreover, accurate dynamic pressure measurements for the prototype is not of great necessity. A lot of publications are available, which testify a good accordance between theoretical and experimental pressure curves, e.g., Ref. [10]. The main results of testing the prototype regard the refuelled amount of NG, especially the efficiency of boosting technology, and, in addition, avoiding the overheating and frosting.

In HYGEN+ Alpha prototype tests, all three stages explained above proved to work properly. Refuelling the target tanks of volume less than 350 L occurs up to 205 bars with the help of the boosting technology. Number of necessary boosting cycles as well as readings of the manometers and of the NG counter are in good accordance with Matlab graphs displayed above.

Heating the heads of compressor cylinders at the compression and boosting stages is of major interest. Figure 6 depicts the temperature measurements of NG in outlet from the compression cylinder at the ending part of both stages. Note that the boosting stage is 10x expanded in time for a better resolution. At the boosting stage, the average ending temperature value reaches 74 °C at linear temperature growth of 1.1 °C /min. The simulation (Fig. 5c) predicts 72 °C and approximately the same growth of 1.1 ± 0.1 °C/min.

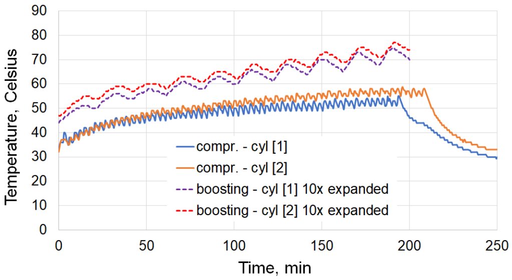

Fig. 6. Temperature measurements from compression and boosting stages with HYGEN+ Alpha prototype.

An important parameter for the compressor type device is its power consumption. As measured, the total electrical consumption of the HYGEN+ Alpha prototype to fill a target tank of 240 L from 10 to 205 bars is 2.04 kWh, whereas from 80 to 205 bars – 1.12 kWh. Regarding the whole refuelling process, the gas storage stage has to be added. It takes ca. 48 hours and consumes 34.8 kWh.

4. DISCUSSION

Matlab simulation allows creating mathematical models for all three stages. At the compression and boosting stages, the main attention is paid to gas temperature growth in the compression cylinder. Inlet NG mass portion of each compression cycle at the boosting stage is significantly larger than that at the compression stage that results in more intense heating of the heads of compression cylinders. The parameters of cooling fans are chosen by first-order approximation of overheated surface and by using a fan calculator. Inconsistency between the theory and the practice turns out to be only 3 % in ending temperature values (72 °C vs. 74 °C). In relation to that, we predicted a bit lower theoretical value due to a simplified theoretical model, which accounts the temperature equilibrium between the gas and thermal bodies. All obtained temperature data are in a safety region and can be corrected in practice by choosing the fans of different parameters. A slight rise in temperature of the receiver cylinder at the compression and boosting stages is observed in simulation as well as in practice. It causes no threats but is the reason why refuelling is worth to be a little over-pressured.

At the free flow stage, a well-known phenomenon is a rapid temperature decrease below zero Celsius degrees. It occurs in the donor cylinder due to gas state equations, whereas in the receiver cylinder due to acting the Joule-Thomson effect within a non-ideal gas. With the particular VFA HYGEN+ the parameters are chosen so that the hydrate formation line may be crossed during a too short period of time to create the hydrates. Regarding the receiver cylinder, in the first few seconds of filling the temperature of gas inside the cylinder is usually below zero Celsius degrees. In practice, we use the mesh filter in the receiver inlet to convince that hydrates have not formed in this critical location.

The hydraulic boosting stage that is considered to be an innovation in VFA devices comes across the technical problem not to damage the hydraulic pump by inlet overpressure. This pressure in the first boosting cycle typically is 80–120 bars, which is considerably larger than the allowed maximal inlet pressure of ca. 50 bars. In the particular VFA, it is solved by supplying the remaining mid-pressure gas from the storage cylinder in a point of time after the hydraulic pump starts to fill the compression cylinder with a working liquid. Thus, the remaining gas causes pressure on the outlet of hydraulic pump.

We noticed that due to physical reasons the boosting stage at too low NG pressure in the storage cylinders became inefficient, especially, in terms of the consumed electric power versus the transferred NG mass. It occurs only when filling very large target tanks. With target tanks less than 350 L refuelling up to full 205 bars is still cost-effective.

5. CONCLUSIONS

The company from Latvia Hygen Ltd. has designed an innovative technology of the hydraulic piston employment in natural gas and biogas compression, allowing one to produce various cost-effective and convenient high-pressure gas storage and vehicle fuelling appliances. When designing an Alpha prototype of a particular gas compression and boosting device, it is highly important to predict thermodynamic characteristics, especially those which indicate possible overheating or frosting. Matlab simulation can give a wide spectrum of numerical results, which are in line with practice, and helps choose parameters and necessary installations to avoid overheating or frosting in critical points. Moreover, it is possible to perform computer simulation of the VFA device for hydrogen enriched natural gas fuel (HCNG) with different hydrogen content [11], [12]. The use of HCNG becomes more and more topical in today’s world due to applying hydrogen technologies to enforce the Paris Agreement on climate change [13], as stated by the European Commission in 2020 [14], [15].

ACKNOWLEDGEMENTS

The research has been supported by the European Regional Development Fund project “Competence Centre of Mechanical Engineering”, contract No.1.2.1.1/18/A/008 signed between the Competence Centre of Mechanical Engineering and the Central Finance and Contracting Agency, Research No. 3.1 “Additional research and integration of the technology of hydraulic piston, aiming to develop and demonstrate economically efficient compressed natural gas smart commercial vehicle fuelling appliance". Our special gratitude to Gaspard Bouteau, PhD, Research Engineer, who conducted research in Engie Lab CRIGEN.

Scientific co-authorship of the Laboratory of Materials for Energy Harvesting and Storage, ISSP UL has been supported by the Ministry of Economics of the Republic of Latvia, project LAGAS No VPP-EM-INFRA-2018/1-0003.

REFERENCES

1. Directive 2014/94/EU of the European Parliament and of the Council of 22 October 2014 on the deployment of alternative fuels infrastructure. *Official Journal of European Union* 2014: L 307/1.
2. *Natural and Renewable Gas: Joint Call to Accelerate the Deployment of Refuelling Infrastructure*. (n.d.). (Accessed 15 February 2020). Available at https://www.ngva.eu/medias/joint-call-for-the-acceleration-of-the-deployment-of-natural-and-renewable-gas-and-its-refuelling-infrastructure-across-the-eu-pr/
3. World Intellectual Property Organisation. (Accessed 16 February 2020). Available at https://patentscope.wipo.int/search/en/detail.jsf?docId=WO2009035311&_cid=P11-K6YVV3-37117-1
4. Hygen Ltd., Company from Riga, Latvia. (n.d.). (Accessed 18 May 2020). Available at http://www.hygengroup.com
5. MathWorks Help Center. (Accessed 10 March 2020). Available at https://www.mathworks.com/help/simulink/, https://www.mathworks.com/help/physmod/simscape/index.html
6. Kuntz, K.J. (1994). *Modeling the fast fill process in natural gas vehicle storage cylinders*. Institute of Gas Technology, Chicago, USA, Corpus ID: 108118392. Available at https://www.semanticscholar.org/paper/Modeling-the-fast-fill-process-in-natural-gas-Kountz/3e40bdba523381ef3dd5bff7e9036943fb75218d
7. Tarom, N., Mofazzal Hossain, Md., & Azar, R. (2018). A New Practical Method to Evaluate the Joule–Thomson Coefficient for Natural Gases. *J. Petrol Explor. Prod. Technol.*, *8*, 1169–1181, DOI: 10.1007/s13202-017-0398-z
8. Maric, I. (2005). The Joule-Thomson Effect in Natural Gas Flow-Rate Measurements. *J. Flow Measurement and Instrumentation*, *16*, 387–395, DOI: 10.1016/j.flowmeasinst.2005.04.006
9. Stego Connect, Inteligent Condition Management, Germany (Accessed 10 March 2020). Available at https://www.stego-group.com/nc/services/calculation-tools/cooling-calculation/
10. Dutton, J.C., & Coverdill, R.E. (1997). Experiments to Study the Gaseous Discharge and Filling of Vessels. *Int. J. Engineering Education, 13* (2), 123–134.
11. Kahraman, N., Akansu, S.O., & Aydin, K. (2009). Investigation of Combustion Characteristics and Emissions in a Spark Ignition Engine Fuelled with Natural Gas-Hydrogen Blends. *International Journal of Hydrogen Energy*, *34* (2), 1026–1034.
12. Morrone, B., & Unich., A. (2009). Numerical Investigation on the Effects of Natural Gas and Hydrogen Blends on Engine Combustion. *International Journal of Hydrogen Energy, 34* (10), 4626–4634.
13. Paris Agreement of Climate Change, Council of the European Union (Accessed 18 May 2020). Available at https://www.consilium.europa.eu/en/policies/climate-change/paris-agreement/

14. Communication from the Commission to the European Parliament, the Council, the European Economic and Social Committee and the Committee of the Regions. Powering a climate-neutral economy: an EU Strategy for Energy System Integration. Available at https://op.europa.eu/en/publication-detail/-/publication/5ba29377-c135-11ea-b3a4-01aa75ed71a1/

15. Communication from the Commission to the European Parliament, the Council, the European Economic and Social Committee and The Committee of the Regions. A hydrogen strategy for climate-neutral Europe. Available at https://op.europa.eu/en/publication-detail/-/publication/5602f358-c136-11ea-b3a4-01aa75ed71a1/

LATVIAN JOURNAL OF PHYSICS
AND TECHNICAL SCIENCES
2020, N 5

DOI: 10.2478/lpts-2020-0024

FEATURES OF ELECTRICITY DISTRIBUTION USING ENERGY STORAGE IN SOLAR PHOTOVOLTAIC STRUCTURE

Y. Veremiichuk[1], O. Yarmoliuk[1], A. Pustovyi[1],
A. Mahnitko[2], I. Zicmane[2]*, T. Lomane[2]

[1]National Technical University of Ukraine
"Igor Sikorsky Kyiv Polytechnic Institute",
37, Prosp. Peremohy, Kyiv, 03056, UKRAINE
[2]Riga Technical University, Institute of Power Engineering,
12/1, Azenes Str., Riga, LV-1048, LATVIA
*e-mail: zicmane@eef.rtu.lv

The intensive development of renewable energy, especially solar power and wind power plants, poses risks of disrupting the balance reliability of the grid. There is the need to develop electricity storage system area, first of all, due to the global tendency to increase the demand for electricity and the number of electricity generation from renewable sources. The issue of guaranteeing electricity supply to the consumer operating in the autonomous renewable source – energy storage device – consumer system is the main criterion when selecting the installed capacity of the generator on the basis of renewable sources and energy storage device capacity. Also, the application does not allow reducing voltage fluctuations in the renewable sources – the consumer system.

Keywords: *Energy storage, rechargeable batteries, renewable energy, solar photovoltaic.*

1. INTRODUCTION

The past decade has seen strong growth in the deployment of renewable energy technologies, with the power sector leading the way thanks to sharp cost reductions for solar photovoltaic (PV) and wind power. In the Stated Policies Scenario [1], nearly 8 500 GW of new power capacity is added globally by 2040, of which two-thirds is renewables. Renewables account for the majority of capacity grows in most regions. This includes about 80 % of additions in the European Union and China, but they provide less than half of additions in Southeast Asia and the Middle East. Solar PV provides the largest share of renewable capacity additions in most regions, including China and India.

In the Sustainable Development Scenario, renewables account for around 80 % of capacity additions in all regions, complemented mainly by nuclear power and carbon capture technologies.

Globally, electricity demand is projected to grow by over 20 % over the next decade, but flexibility – the ability of the power system to quickly adapt to changes in power supply and demand – will grow by some 80 %. Flexibility will therefore be the cornerstone of future electricity systems. It will be met not only by traditional sources of flexibility – such as conventional power plants and electricity grids – but also by new sources of flexibility, including battery storage and demand-side response, which are projected to grow fast and contribute to 400 GW by 2040 (Fig. 1).

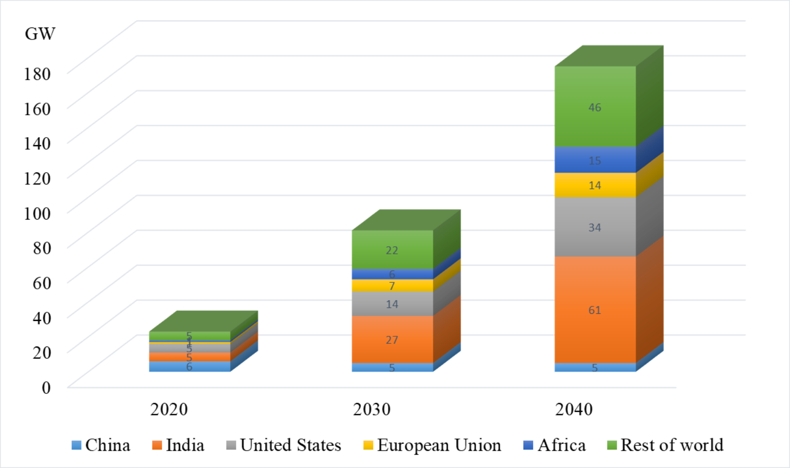

Fig. 1. Installed capacity of utility-scale battery storage systems in the New Policies Scenario, 2020–2040.

Ukraine has not stayed away from world trends. Today, due to the state subsidization of renewable energy sources (RES) electricity producers, there is an intensive development of RES, which are connected to the electricity system at the level of distribution electricity grids, which leads to a gradual transition from a purely centralised (big atomic and fossil fuel power stations) model of electricity supply to combined when part of electricity is generated by dispersed sources.

According to the operational data of the National Energy Commission "Ukrenergo", the total installed capacity was 53042.50 MW in January 2020; RES capacity was 4949.80 MW, and it was distributed according to generation technologies in this ratio (Fig. 2).

The intensive development of renewable energy, especially solar power plants and wind power plants, poses risks of disrupting the balance reliability of the grid. In order to continue the increase of RES share, it is necessary to increase the volume of primary, secondary regulation and substitution reserve.

It is necessary to develop electricity storage systems area, first of all, due to the global tendency to increase the demand for electricity and the number of electricity generation from renewable sources.

With smooth operation, electrical storage systems will contribute to the stable functioning of the grid, reduce network imbalances caused by unbalanced loads from consumers, and maintain the pace of renewable electricity inputs.

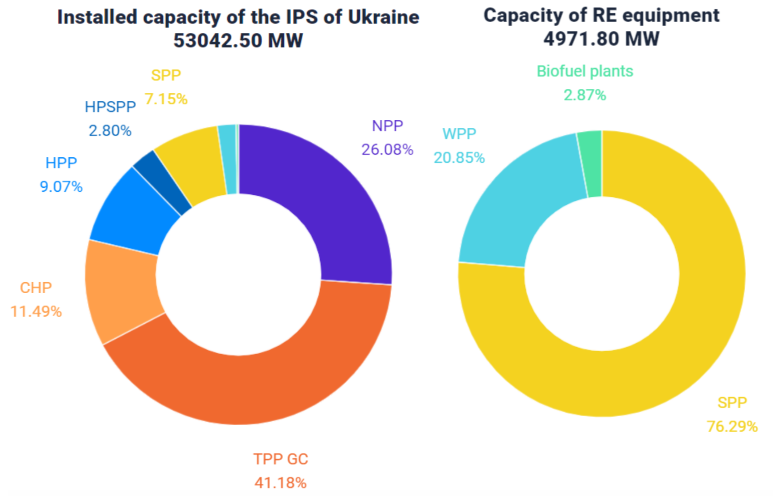

TPP GC – energy generating companies of thermal power plants, NPP – nuclear power plants, CHP – combined heat and power, HPP – hydro power plants, HPSPP – hydro pumped storage power plants, SPP – solar power plants, WPP – wind power plants

Fig. 2. The installed capacity of the integrated distribution system of Ukraine and power of RES equipment [2].

2. THEORETICAL CALCULATIONS

The use of RES has a number of positive qualities that ensure their active development. In particular we can determine no environmental pollution during operation, the need for maintenance and others. Along with the positive properties, there are a number of disadvantages, the main of which is the lack of predictability of generation volumes as a time function and the impact on electricity supply security [3]–[5]. However, by integrating an energy storage device (ES) into the system of a generating set, it can significantly reduce the negative impact of the unpredictable generation factor [6]–[8]. ES application helps accumulate surpluses generated by RES and use the accumulated energy in times of scarcity and / or lack of generation from RES [9].

The issue of guaranteeing electricity supply to the consumer operating in the autonomous RET-ES-consumer system is the main criterion when selecting the installed capacity of the generator on the basis of RET and ES capacity [10]. Also, the application does not allow reducing voltage fluctuations in the RET-consumer system [11], [12].

Analysing the parameters of modern ES, different types of rechargeable batteries (RB), taking into account the specific energy consumption of 30–400 W·h /kg and the number of life cycles of 500–1200, can be considered the most suitable for long-term use in the RES-ES-consumer system. One of the ways to solve the problem of guaranteed electricity supply is to choose ES that allows accumulating all energy excess generated by RES and the consumed load [13], [14]. An important feature of the RES-ES-consumer system is the constant presence of excess generation, which can be used during periods of scarcity and / or absence of RES generation. Determining the ES parameters to cover the needs of the autonomous consumer is important enough and at the same time not sufficiently elaborated. Therefore, the relevant question remains the use of ES in the energy hub [15], which has its own RES and interacts with the grid under different market conditions [16].

It is necessary to consider that there are restrictions that do not allow for the use of all 100 % of stored energy in the RB, which is due to its type [17].

The charge of each RB can be divided into two parts. The first part is the maximum depth of discharge (MDOD) for a certain type of RB, which is a relative value for most types of modern RB. All RB manufacturers and their equipment technical data sheets indicate MDOD as the degree of discharge at which the RB operates the least number of charge / discharge cycles. Though, when the discharge is higher than MDOD, the RB wear rate increases. It will be logical to state that there is a certain relative value of the minimum degree of charge of the RB, which must be permanently stored in the RB MSOC (minimum state of charge). Thus, for each individual type of RB the following expression can be written:

$$MSOC + MDOD = 1\,. \qquad (1)$$

The numerical expression of the energy contained in the RB can be determined by arithmetically multiplying the value of the capacitance RB by the voltage between its terminals. Typically, RB is used to determine the nominal capacity and submit it in A·h. Therefore, it is more convenient to operate the battery charge level rather than its capacity. Depending on the operating modes that are constantly changing (charge discharge), the charge value (amount of stored energy) changes. Since at each point of time we will have different values of the electric charge (A·h), it can be numerically expressed by the dimensionless SOC (state of charge) ratio of the current charge RB to its nominal capacity. Next to the SOC, there is a DOD (depth of discharge) ratio of the RB discharge to its nominal capacity. That is, at any point in time RB can be described by the expression:

$$SOC(t) + DOD(t) = 1\,. \qquad (2)$$

From Eq. (2) it follows that a fully charged RB corresponds to a value $SOC(t) = 1$ and $DOD(t) = 0$. Fully discharged RB – $SOC(t) = 0$ and $DOD(t) = 1$.

From the above we can see that there is a range of charge levels of the RB in which it will work without failure, let us call it NRM (normal run mode). NRM is a range from full charge RB to MSOC, which can be described as follows:

$$NRM \in [MSOC;1]. \qquad (3)$$

In numerical form, NRM can be defined as follows:

$$NRM = 1 - MSOC = MDOD\,. \qquad (4)$$

The change in SOC at successive time intervals can be expressed as a dependency:

$$SOC(t) = SOC(t-1) + \frac{A_{RES}(t) - \left(A_{load}^{DC}(t) + \dfrac{A_{load}^{AC}(t)}{\eta_{inv}} \right)}{V_{bat} C_{bat}}, \qquad (5)$$

where $A_{RES}(t)$ – the amount of energy produced by RES, $A_{load}^{DC(AC)}(t)$ – the amount of energy consumed by the load (the upper indices are applied to DC and AC, respectively), η_{inv} – inverter efficiency, V_{bat} – voltage at terminals of RB array, C_{bat} – RB array capacity.

It should be noted that the selected capacity of the RB array in the entire cycle of operation, with uninterrupted supply of electrical energy to the load, should be in the charged state. This statement can be represented by the expression:

$$\forall SOC(t) = MSOC. \qquad (6)$$

The RB state can be described by the dependence of the SOC invariance criterion:

$$SOC(t_0) = SOC(t_T). \qquad (7)$$

Depending on Eq. (7), the start of the RES work period with RB is the beginning of the calculation cycle. Taking into account Eq. (7), the dependence (5) will be

$$SOC(t_T) = SOC(t_0) + \frac{A_{RES}(t) - \left(A_{load}^{DC}(t) + \dfrac{A_{load}^{AC}(t)}{\eta_{inv}} \right)}{V_{bat} C_{bat}}. \qquad (8)$$

The condition (7), with (8), gives the dependence:

$$\sum_{t=t_i}^{t_T} \left[A_{RES}(t) - \left(A_{load}^{DC}(t) + \frac{A_{load}^{AC}(t)}{\eta_{inv}} \right) \right] = 0. \qquad (9)$$

Dependence (9) makes it possible to determine the necessary value for $A_{RES}(t)$ and to choose the appropriate hardware for its implementation according to the consumer’s needs.

Using dependence (9) in this case it is possible to determine the number of photovoltaic panels of a certain type that will provide the production of electrical energy in volume depending on consumption.

Since it changes randomly, the energy accumulated / transmitted by the RB can be determined when equality (9) is not fulfilled in relation to (7), i.e. an excess / deficit of electrical energy produced by RES. The energy $A_{RES}(t)$ accumulated / released by RB can be determined according to (9) by the dependence of:

$$A_{bat}(t) = A_{RES}(t) - A_{load}^{DC}(t) + \frac{A_{load}^{AC}(t)}{\eta_{inv}}. \qquad (10)$$

Dependence (10) makes it possible to determine the RB capacitance, if it is constant, by dividing the right and left portions of this dependence by $V_{bat}C_{bat}$. However, according to the research, it is known that depending on the charging current $\left(I^{+}\right)$ RB will have a different capacity; depending on the state of charge $SOC(t)$, the voltage at RB array terminals will vary. The capacity of the RB also changes under the influence of the ambient temperature and the lifetime – degradation of the active substances of the RB.

For further use of dependence (10), it is necessary to neglect influencing factors on the result of the RB capacitance value volatility. Therefore, the capacitance of the RB is considered to be the amount of energy that RB contains. We will estimate the amount of this energy by determining the RB charge – $Q(t)$.

The amount of energy that an RB array contains at any given time can be regarded as dependent on the $SOC(t)$. In numerical terms:

$$Q(t) = C_{bat}SOC(t). \tag{11}$$

In Eq. (8), C_{bat} means the current value of the RB capacitance, which cannot be determined during operation.

At each point in time, the RB charge will determine the sum of two components: RB charge at the start of the operation $Q(t_0)$ and all stored energy in the RB at the current time. According to (8) and (10), the following dependence can be obtained:

$$Q(t) = Q(t_0) + \sum_{t=t_i}^{t_T} \frac{A_{bat}}{V_{bat}}. \tag{12}$$

The value of $Q(t)$ according to (12) must be greater, which corresponds only to the fully charged RB state. Achieving this condition is possible by accordingly choosing the value of $Q(t_0)$.

During the whole period of RES operation, depending on the produced energy volume, the RB charge value according to formula (12) may vary from $Q_{\min}$ to $Q_{\max}$. These values can be determined from all the calculated value series as follows:

$$Q_{\min} = \min(Q(t)), \quad Q_{\max} = \max(Q(t)), \quad t = [t_1, t_2 \ldots t_T]. \tag{13}$$

Since the $Q_{\min}$ value must be positive (subject to a constant charge array RB), the minimum charge and the value of the operating range selected as a result C_{bat} must meet the following conditions:

$$Q_{\min} \geq DODC_{bat}, \tag{14}$$

$$Q_{\max} - Q_{\min} \geq NRMC_{bat}. \tag{15}$$

Taking into account Eqs. (14) and (15), we obtain a two-criterion equation:

$$C_{bat} \geq \max\left[\frac{Q_{\max} - Q_{\min}}{NRM}, \frac{Q_{\min}}{MSOC}\right]. \tag{16}$$

The calculation according to dependence (16) can be performed in case of existing consumer's electric load schedule and forecast / statistics on RES electricity generation. The calculation should be performed for typical periods of RES–RB complex use depending on the time of the year, working days and days off, etc. Particular attention should be paid to ensuring that the charge / discharge current RB is limited. The value of the RB capacity according to the calculation results should satisfy all selected periods of the RES–RB complex usage.

3. EXPERIMENTAL RESULTS

Let us calculate the choice of ES power for the distribution electrical network area, in which the SPP is integrated (Fig. 3).

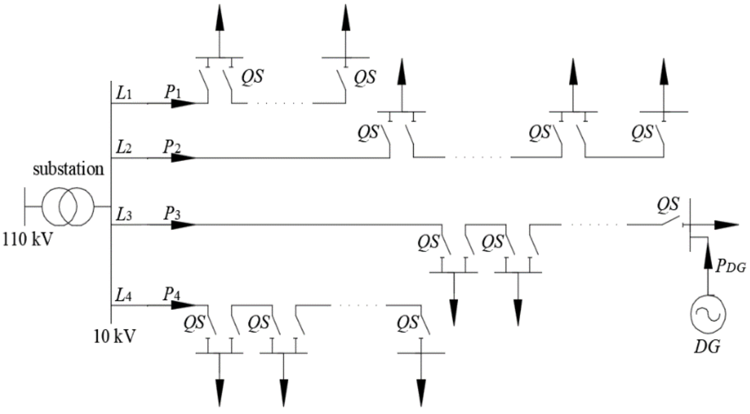

Fig. 3. An example of distribution electrical network area.

The 110/10 kV electrical substation supplies four 10 kV L_1–L_4 distribution lines, the load of which is modelled by the built-in random number function in MS Excel software.

The calculation carried for ES power choice for two scenarios:

- integrated distribution system (IDS) sets limits on the possible SPP generation power flow through a 110/10 kV substation;
- IDS sets a load schedule requirement for the distribution network area under consideration.

Consider a situation where IDS sets a limit on the possible flow of excess SPP-generated power through a substation. Let us analytically show this by the following expression:

$$P_{Sub} = P_1 + P_2 + P_3 + P_4 - P_{DG} \geq 0\,, \qquad (17)$$

where P_1, P_2, P_3, P_4 are the load of the 10 kV distribution lines L_1, L_2, L_3 and L_4, respectively, kW; P_{DG} is the power generated by the SPP integrated into the distribution network, kW.

Under condition (2), for the considered area of the distribution network an electricity accumulator (EA) will accumulate undelivered (surplus) electricity SPP with the possibility of further release within the IDS limit set.

The amount of electricity A released for a certain period of time Δt into the distribution network is calculated by the expression:

$$A_i = P_i \Delta t\,. \qquad (18)$$

The total load of the distribution network of 10 kV area and the SPP generation schedule, which is integrated into the grid, are shown in Fig. 4. The SPP generation schedule is taken from the existing station and the electricity generated from the grid is calculated using Eq. (18).

During the day, the distribution network (L_1–L_4 lines) consumed $A_{Sub} = 20893$ kWh and generated SPP – ADG =17753.03 kWh.

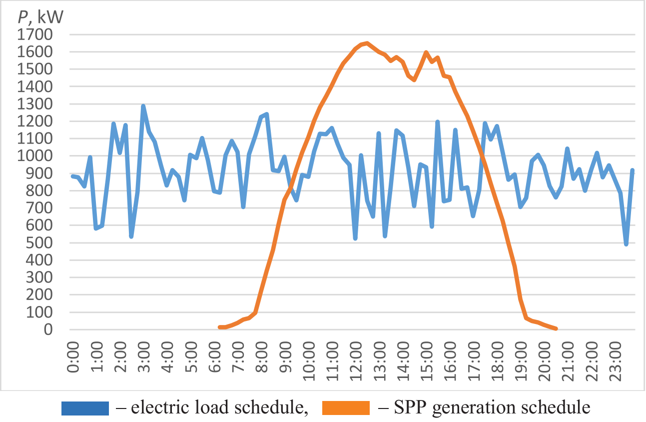

Fig. 4. Graph plots of total distribution network load and SPP generation for one day.

To obtain the data on the 10 kV substation busbar load, taking into account the generation of SPP that is integrated into the distribution network, Eq. (19) is used.

$$P_{Sub} = P_1 + P_2 + P_3 + P_4 - P_{DG} \tag{19}$$

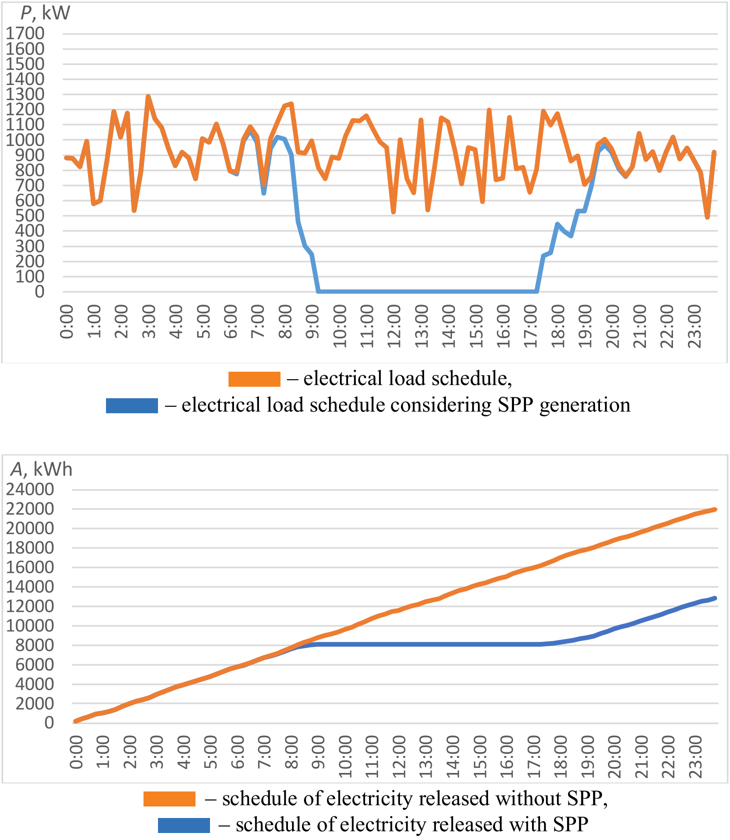

Fig. 5. Graph plots of electricity consumption, taking into account the IDS constraints and sufficient SPP generation (a – timetable for the IDS limitation on power flow; b – comparative graph of electricityconsumption with and without SPP in selected grid area).

The integration of the SPP into the distribution network area under consideration (Fig. 3) has a significant impact on the 10 kV substation busbar load. In the absence of SES, the amount of electricity released from the 10 kV substation busbar into the network per day was 20893 kW·h, and with the appearance of the SPP – 7578.23 kW·h.

Taking into account the IDS constraints and sufficient SPP generation, which from 10.00 to 17.00 can completely satisfy the electricity needs of the distribution network area, there is possibility and necessity of generated electricity accumulation from SPP. Graphically, it is demonstrated in Fig. 5.

The total amount of accumulated electricity in EA will be 4174.756 kW·h per day.

In the presented case, when the IDS establishes a restriction on the possible power flow (excess of SPP generated power) through the substation, the EA power should be selected based on the data obtained on the total accumulated electricity per day. In this situation, the EA power should not be less than 4174.756 kW·h, this value is brought to the nearest standard – 4200 kW·h.

Let us consider the second scenario, in which the IDS sets a load schedule requirement for the distribution network area (Fig. 3).

The minimum value of electrical load is $P_{\min} = 540.1$ kW and accordingly the maximum value is $P_{\max} = 1160.1$ kW. The total amount of electricity released by the 10 kV substation busbar should be 20816.5 kW·h per day.

In order to comply with the established load schedule (Fig. 6), the 10 kV substation busbar, which is the power supply point for the four lines and the SPP, EA must be integrated into the SPP structure.

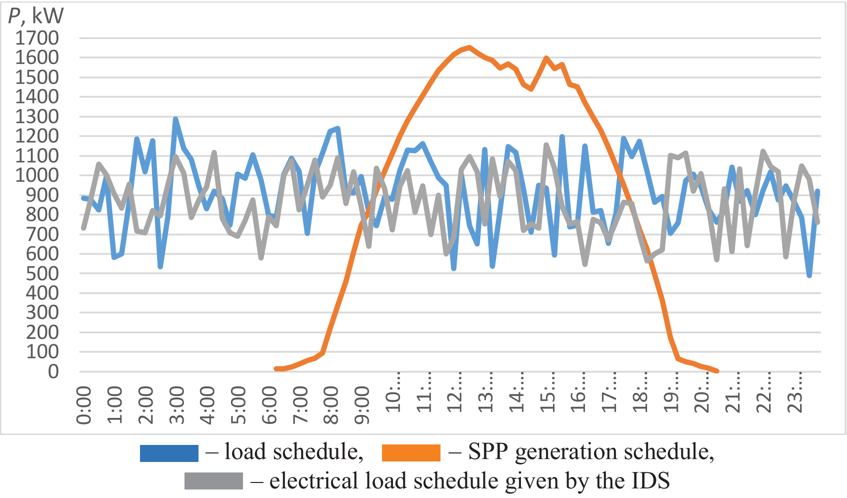

Fig. 6. Combined load and generation schedule for the distribution network area.

We calculate the load at time moment on EA terminals by Eq. (20).

$$P_{\text{HE}} = P_{Sub} - P_1 - P_2 - P_3 - P_4 + P_{DG}\,. \quad (20)$$

Taking into account the limitation on electricity consumption from the 10 kV substation busbar (Fig. 6), Fig. 7 shows the “charge-discharge” process of an electric drive for balancing in the selected distribution network area.

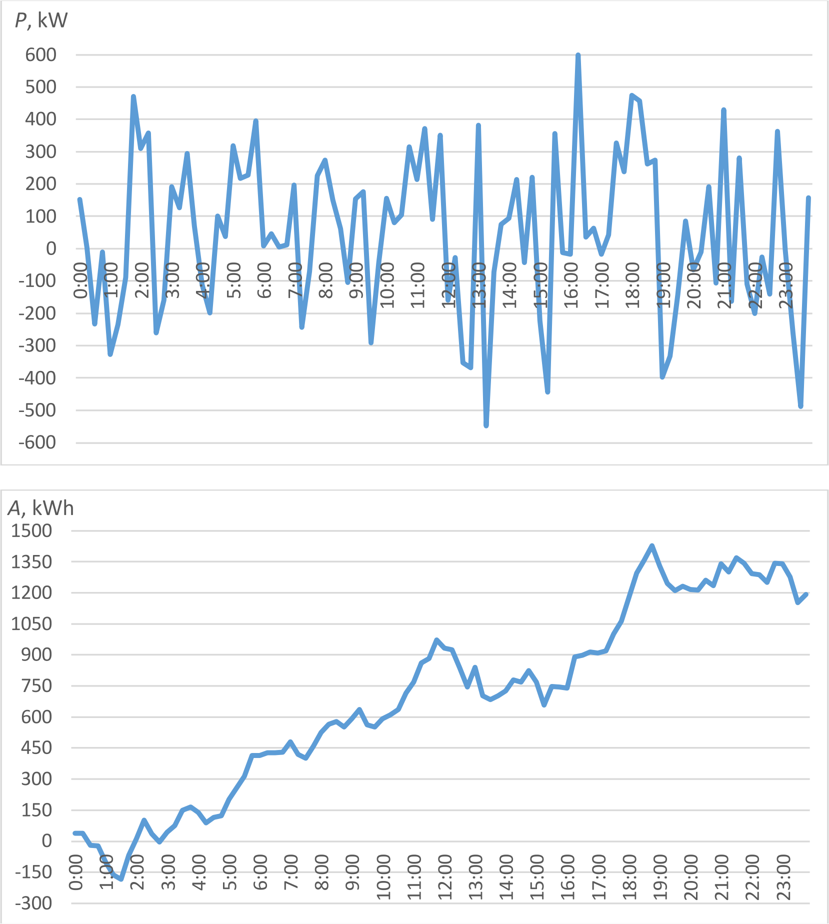

Fig. 7. EA charge and discharge process (a – power; b – electricity amount).

Figure 7a demonstrates both positive and negative power values. Positive values reflect the EA charge process due to the appearance of excess power, and negative values reflect the EA discharge process due to the system power lack.

After analysing the given data and the EA work schedule, its charge and discharge are $Q_{\max} = \grave{A}_{\max} = 1428.5$ kW·h, $Q_{\min} = \grave{A}_{\min} = -184.5$ kW·h.

Based on the values of charge and discharge, it is possible to calculate the required EA power using Eq. (16):

$$A_{EA} \geq \max\left[\frac{Q_{max}-Q_{min}}{NRM} : \frac{Q_{min}}{MSOC}\right] =$$
$$= \max[1792.22;-1845] = 1792.22 \text{ kWh}.$$

As a result of the calculation, the optimum EA standard power can be selected:

$$A_{EA} = 1800 \text{ kW·h}.$$

The various renewable energy sources that use energy storage in their structure can be considered the integrated power systems for expanding the network node in the electricity grid. Developing and implementing approaches to optimize the functioning of such energy hubs are a promising project in the context of sustainable development of Ukraine’s energy sector.

4. CONCLUSIONS

The use of renewable energy sources in the grid imposes certain features on IDS operation, in part of electricity consumption mode formation and can be implemented using probabilistic prediction methods and algorithms of artificial neural networks.

The use of energy storage will allow RES entities to comply with IDS requirements regarding electricity losses, which will, as a result, meet the operational safety standards of the electricity grids.

Using the procedure of the optimal capacity calculating for the complex “renewable source-battery”, for each scenario EA optimal power allows providing the optimum quality of electricity. The simulation also found that the load schedule constraints for the PV distribution area required less energy storage than the restriction on the possible power flow.

REFERENCES

1. International Energy Agency. (n.d.). Available at https://www.iea.org/reports/world-energy-outlook-2019/
2. Installed Capacity of the IPS of Ukraine and Capacity of Renewable Energy Equipment. (n.d.). Available at https://ua.energy/installed-capacity-of-the-ips-of-ukraine/
3. Du, E., Zhang, N., Hodge, B.-M., Wang, Q., Lu, Z., Kang, C., & Xia, Q. (2018). Operation of a High Renewable Penetrated Power System with CSP Plants: A Look-ahead Stochastic Unit Commitment Model. *IEEE Transactions on Power Systems*, *34* (1), 140–151. Doi:10.1109/tpwrs.2018.2866486.
4. Hui, G., Tiejun, L., Xin, S., Hong, Y., & John, M.C. (2016). Energy-efficient resource allocation for massive MIMO amplify-and-forward relay systems. In *16th International Conference on the European Energy Marke*t, 2016 (pp. 2771–2787). Doi: 10.1109/ACCESS.2016.2570805.
5. Veremiichuk, Y., Zamulko, A., Zaichenko, S., Mahnitko, A., Berzina, K., & Zicmane, I. (2018). Analysis of electric energy supply security attached to renewable energy sources implementation. In *X International Conference on Electrical and Power Engineering* (pp. 0977–0981), 18–19 October 2018. Iaşi, Romania.
6. Wang, Z., Luo, D., Li, R., Zhang, L., Liu, C., Tian, X., & He, J. (2017). Research on the active power coordination control system for wind/photovoltaic/energy storage. In *IEEE Conference on Energy Internet and Energy System Integration*, 26–28 November 2017. Beijing, China. Doi:10.1109/ei2.2017.8245403.
7. Wang, X., & Liu, Y. (2017). Analysis of energy storage technology and their application for micro grid. In *International Conference on Computer Technology, Electronics and Communication*, 19–21 December 2017. Dalian, China. Doi:10.1109/icctec.2017.00215.
8. Berry, I., & Heinzmann, J. (2016). Economics of energy storage for dispatchable solar. In *IEEE Power and Energy Society General Meeting*, 17–21 July 2016. Boston, USA. Doi:10.1109/pesgm.2016.7741165.
9. Yakymenko, Y.I., Sokol, Y.I., Zhuikov, V.I., Peterheria, Y.S., & Ivanin, O.L. (2001). *Renewable energy at local sites*. Ukraine: Kyiv: Polytechnics.
10. Kleinberg, M., Mirhosseini, N.S., Farzan, F., Hansell, J., Abrams, A., Katzenstein, W., & Jafari, M.A. (2014). Energy Storage Valuation under Different Storage Forms and Functions in Transmission and Distribution Applications. *Proceedings of*

the IEEE, *102* (7), 1073–1083. Doi:10.1109/jproc.2014.2324995.

11. Zaharov, A.M. (2014). Reduction of Voltage Deviations at Places of Connection of Powerful Solar Power Plants to Power Grids. *Tekhnichna elektrodynamika*, *5*, 44–46.
12. Hao, C., Yanbing, J., Jin, Z., Yanfang, Z., Gang, L., & Dong, X. (2019). Energy storage frequency regulation energy management strategy based on k-means analysis. In *IEEE 3rd International Conference on Green Energy and Applications*, 16–18 March 2019. Taiyuan, China. Doi:10.1109/icgea.2019.8880782.
13. Jing, Li.J., Wei, W., & Xiang, J.A. (2012). Simple Sizing Algorithm for Stand-Alone PV/Wind/Battery Hybrid Microgrids. *Energies*, *5*, 5307–5323.
14. Ponnambalam, K., Saad, Y.E., Mahootchi, M., & Heemink, A.W. (2010). Comparison of methods for battery capacity design in renewable energy systems for constant demand and uncertain supply. In *7th International Conference on the European Energy Market*, 23–25 June 2010. Madrid, Spain. Doi:10.1109/eem.2010.5558745.
15. Veremiichuk, Y., Prytyskach, I., Yarmoliuk, O., & Opryshko, V. (2019). Energy sources selection for industrial enterprise combined power supply system. In *IEEE 6th International conference on Energy Smart Systems*, 17–19 April 2019 (pp. 283–288). Ukraine, Kyiv.
16. Veremiichuk, Y. Berzina, K., Zicmane, I., Mahnitko, A., & Patel, D.K. (2019). Optimal Power Flow in Power System in Latvian Market Conditions. *International Multidisciplinary Scientific GeoConference Surveying Geology and Mining Ecology Management*, *19* (4.1), 369–375.
17. Root, C., Presume, H., Proudfoot, D., Willis, L., & Masiello, R. (2017). Using battery energy storage to reduce renewable resource curtailment. In *IEEE Power & Energy Society Innovative Smart Grid Technologies Conference*, 23–26 April 2017.Washington, USA. Doi:10.1109/isgt.2017.8085955.

LATVIAN JOURNAL OF PHYSICS
AND TECHNICAL SCIENCES
2020, N 5

DOI: 10.2478/lpts-2020-0025

ESTIMATION OF ELECTROMAGNETIC COMPATIBILITY BETWEEN DVB-T/DVB-T2 AND 4G/5G IN THE 700 MHZ BAND FOR CO-CHANNEL CASE

G. Ancans[1*], E. Stankevicius[2], V. Bobrovs[1], G. Ivanovs[1]

[1]Institute of Telecommunications, Riga Technical University,
12 Azenes Str., Riga, LV-1048, LATVIA
[2]Vilnius Gediminas Technical University,
Sauletekio al. 11, Vilnius, LT-10223, LITHUANIA
*e-mail: guntis.ancans@rtu.lv

The 694–790 MHz band (700 MHz) known also as the second digital dividend was allocated to the mobile radiocommunication service on a primary basis in Region 1 and identified to International Mobile Telecommunications by the World Radiocommunication Conference 2012 (WRC-12). The designation of mobile service in Europe and other countries of Region 1 in 700 MHz band was obtained after the World Radiocommunication Conference 2015 (WRC-15). Administrations of Region 1 will be able to plan and use these frequencies for mobile networks, including IMT. The goal of this study is to estimate the electromagnetic compatibility of Digital Video Broadcasting – Terrestrial (DVB-T/DVB-T2) and LTE (Long Term Evolution) technology operating both in 700 MHz band. The study assumes frequency division duplex (FDD) channel arrangement of 703–733 MHz (for uplink) and of 758–788 MHz (for downlink).

The model contains two parts: a DVB-T/DVB-T2 system and LTE mobile broadband network. Co-channel scenario is considered in this paper, and possible impact of DVB-T/DVB-T2 on LTE base stations (receivers) is also investigated. The Monte Carlo simulations within SEAMCAT software and the Minimum Coupling Loss (MCL) method are used for interference investigation. The coordination trigger field strength value predetermined by GE06 Agreement is also used in this study. The Monte Carlo method presents more relaxed electromagnetic compatibility scenario in comparison with the MCL method. For SEAMCAT simulations, ITU-R P.1546-5 radio propagation model is used.

The obtained results present the required minimum separation distance between DVB-T/DVB-T2 and LTE networks in the 694–790 MHz in order to provide the necessary performance of LTE mobile network.

Keywords: *4G, 5G, DVB-T/T2, DTTB, electromagnetic compatibility, IMT, interference, LTE, mobile communication, Monte Carlo, NR, SEAMCAT.*

1. INTRODUCTION

The World Radiocommunication Conference 2012 approved Resolution 232 (WRC-12) relating to the allocation of the 694–790 MHz frequency band (700 MHz) to the mobile radiocommunication service in Region 1 on a co-primary status with other primary services and identified the band to International Mobile Telecommunications (IMT) [1].

According to Resolution 232 (WRC-12), ITU-R has to study the compatibility between the mobile service and other services currently allocated in the 694–790 MHz [2]. The frequency band can be utilised only after all mandatory electromagnetic compatibility studies have been finished. This study provides the estimation of electromagnetic compatibility of Digital Video Broadcasting – Terrestrial (DVB-T and DVB-T2) operating in the 700 MHz band and LTE700. The study identifies the necessary minimum separation distance between these systems in the 700 MHz band to maintain the minimum performance level of the LTE700 base stations (BS).

Three different ways of investigation are used in this paper for electromagnetic compatibility evaluation: the Minimum Coupling Loss (MCL) method, calculations of a coordination trigger field strength value predetermined by GE06 Agreement, and Monte Carlo simulations method using SEAMCAT.

The authors have identified that studies on estimation of compatibility of DVB-T/T2 and LTE700 are performed within the JTG-4-5-6-7 study group of ITU-R [3]. The studies in [3] present co-channel interference calculation results from Digital Terrestrial Television Broadcasting (DTTB) transmitters and GE06 Plan entries installed into IMT uplink. For protection of receivers of base stations, the *I/N* criteria were used in these studies. The studies demonstrate that coupling distances of up to 427 km and 269 km for High Power and Medium Power DTTB transmitters, respectively, would be required to keep safe the IMT base station receiver for 99 % time at a target *I/N* of –6 dB and with no additional discrimination by cross-polarization or receiving antenna directivity.

Unlike the aforementioned studies, the present research is based on the MCL method, Monte Carlo method, and a coordination trigger field strength value predetermined by GE06 Agreement. Different values of e.r.p. (Effective Radiated Power), frequencies, compatibility evaluation methodologies etc. were used in the studies [3]. This paper involves important contribution of compatibility evaluation of DVB-T/T2 and LTE700 operating in the 694–790 MHz. Evolved versions of LTE are planned to be used as a basis for development of 5G mobile services and networks in 700 MHz band.

The paper is organised as follows. The second section is devoted to the technical characteristics of LTE/LTE-A and DVB-T/DVB-T2. The third section describes the interference scenario. The fourth section is dedicated to the compatibility analysis and results. In the last section conclusions are drawn.

2. TECHNICAL CHARACTERISTICS

This study provides an assumption of a frequency division duplex (FDD) channel arrangement of 2×30 MHz: 703–733 MHz for uplink and of 758–788 MHz for downlink [4], [5].

For 5G NR (New Radio) non-AAS (non-Active Antenna Systems), the 3GPP defined transmit and receive characteristics for UE (User Equipment) and BS (Base Station) (TS38.101-1 and TS 38.104) that are generally comparable to those defined for LTE (TS36.101 and TS 36.104). Taking into account that in-band and out-of-band e.i.r.p. (Equivalent Isotropically Radiated Power) of the NR signal transmitted by the NR non-AAS base station does not exceed the limits, which apply to LTE carrier, the NR signal does not create more interference to other services in the same band or to adjacent band services than an LTE signal using the same bandwidth and transmitting at the same power [6].

A. Parameters of LTE/LTE-A

The LTE/LTE-A parameters used in this study are derived from inputs to JTG 4-5-6-7 task group from WP5D working group for IMT (LTE700) [7] and ITU-R Report M.2292-0 [8].

Mobile service (LTE700) base station parameters used in this study are given in Table 1.

Table 1. Characteristics of LTE Base Station

Parameter	**Value**
Transmitting (Tx) frequency	763 MHz
Receiving (Rx) frequency	708 MHz
Channel bandwidth	10 MHz
Signal bandwidth	9 MHz
Maximum output power	46 dBm
e.i.r.p.	58 dBm
Antenna height	30 m
Antenna gain	15 dBi
Base station antenna pattern	3GPP Tri-sector antenna (60º)
Feeder loss	3 dB
Antenna downtilt	3º
Receiver noise figure	NF=5 dB
Cell size/radius	8 km (rural environment)
Sectorization	3 sectors
Antenna polarization	± 45º
Reference sensitivity	–101.5 dBm
Noise floor	$10 \cdot \log_{10}(k \cdot T_0 \cdot B) + NF =$ –99.4 dBm
I/N	–6 dB
Receiver blocking mask	Table 7.6.1.1-1 of 3GPP TS 36.104 (V14.3.0)

The main parameters of LTE user equipment are provided in Table 2.

Table 2. Characteristics of LTE User Equipment

Parameter	Value
Transmitting (Tx) frequency	708 MHz
Receiving (Rx) frequency	763 MHz
Channel bandwidth	10 MHz
Maximum output power, e.i.r.p	23 dBm
Antenna height	1.5 m
Antenna gain	–3 dBi
Body loss	4 dB
Receiver noise figure	NF=9 dB
Reference sensitivity	–95.5 dBm
Number of active LTE UE per BS cell	3

B. Parameters of DVB-T/DVB-T2

The DVB-T and DVB-T2 characteristics used in this study are derived from inputs to JTG 4-5-6-7 task group from WP6A working group for DTTB [9]. The DVB-T and DVB-T2 parameters used in this paper are provided in Table 3.

Table 3. Characteristics of DVB-T / DVB-T2

Parameter	Value
Transmitter power e.r.p.	200 kW (High Power) 5 kW (Medium Power)
Transmit power e.i.r.p.	85.15 dBm (High Power) 69.15 dBm (Medium Power)
Tx/Rx frequency	706 MHz (TV channel 50)
Bandwidth	8 MHz
Signal bandwidth	7.6 MHz for DVB-T 7.77 MHz for DVB-T2
Tx antenna height	300 m (High Power) 150 m (Medium Power)
Tx antenna gain	0 dBi
Rx antenna gain (including feeder loss)	9.15 dBi
Rx antenna height	10 m
Antenna downtilt	1º (High Power) 1.6º (Medium Power)
Feeder loss	4 dB
Rx antenna pattern	Horizontal: omnidirectional BT.419
Rx sensitivity (P_{min} at the receiver input)	–77.17 dBm for DVB-T –79.07 dBm for DVB-T2
Rx noise level	–98.16 dBm for DVB-T –99.07 dBm for DVB-T2
DVB-T coverage range	70.53 km (High Power) 32.11 km (Medium Power) (using P.1546-4 with 10 m clutter)
Receiver noise figure (NF)	7 dB for DVB-T 6 dB for DVB-T2

In this study, *I/N= –6 dB* protection criteria are used to investigate the interference from DVB-T/T2 transmitters to LTE base station receivers (uplink).

3. INTERFERENCE SCENARIO

It is assumed that LTE700 network works in a 10 MHz channel (BS Rx frequencies between 703 MHz and 713 MHz). DVB-T/T2 station operates in TV channel 50 (frequencies between 702 MHz and 710 MHz). Co-channel interference case is presented in Fig. 1.

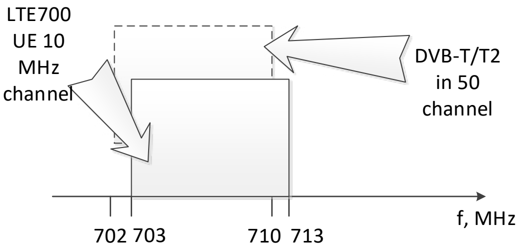

Fig.1. Interference scenario model in the frequency plane.

The interference scenario where DVB-T/T2 transmitter interferes LTE700 receiving stations (uplink) in a co-channel is evaluated in this paper. Simulation scenario in SEAMCAT is given in Fig. 2.

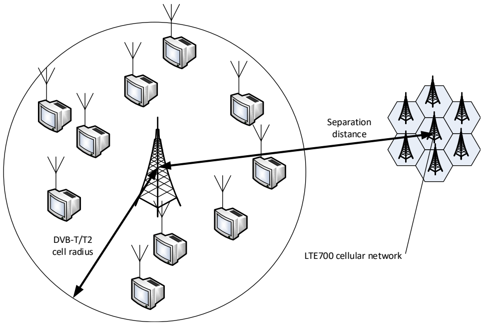

Fig. 2. SEAMCAT simulation scenario.

This contribution focuses on a scenario as shown in figure above: DVB-T/T2 transmitter interference into mobile service BS receivers. In our simulations, we address the case where LTE700 receiving BSs (cellular network) are randomly located at the DTTB cell edge in a rural environment.

4. COMPATIBILITY ANALYSIS AND RESULTS

According to Ericsson paper [8], LTE will explicate in a way of providing coverage for mobile users. 5G networks will comprise LTE access based on Orthogonal Frequency Division Multiplexing (OFDM) along with new radio interfaces.

A. MCL Method Calculation Results

For initial estimation of compatibility, MCL calculations are used. The minimum path loss of MCL method, $L_{Req\_path\_loss}$, between the interfering DVB-T/T2 transmitter (I_t) and the victim LTE700 base station receiver (V_r) to secure that there is no harmful interference is derived from

$$L_{Req\_path\_loss} = P_{DTTB\_e.i.r.p.\_Tx} + G_{BS\_Rx} - P_{I\_BS\_Rx}, \tag{1}$$

where $P_{DTTB\_e.i.r.p.\_Tx}$ – *e.i.r.p.* of the interfering DVB-T/T2 transmitter (dBm); G_{BS_Rx} – victim LTE700 base station receiver antenna gain (dBi). In these MCL calculations, DVB-T/

T2 Tx frequency is 706 MHz. The interference strength at the LTE700 base station receiver, $P_{I\_BS\_Rx}$, is derrived from

$$P_{I\_BS\_Rx} = P_{n\_BS\_Rx} + I/N, \tag{2}$$

where $P_{n\_BS\_Rx}$ – noise power at the LTE700 base station receiver ; *I/N* – interference to noise ratio.

$$P_n = NF + 10\log_{10}(k \cdot T_0 \cdot B), \tag{3}$$

where P_n – receiver noise input power (dBW); *NF* – receiver noise figure (dB); k – Boltzmanns's constant (k=1.38×10^{-23} J/K); T_0 – absolute temperature T_0=290 K; B – receiver noise bandwidth (7×10^6 Hz for a 10 MHz LTE700 channel). The minimum path loss between the DVB-T/T2 (High Power) and the LTE700 base station receiver is

$$L_{Req\_path\_loss\_High\_Power} = 85.15\ dBm/8\ MHz + 15\ dBi \\ -(-106.5\ dBm/7\ MHz) = 206\ [dB]. \tag{4}$$

The path loss value is converted into a coupling distance using the ITU-R Recommendation P.1546-5. The allowable interference level emitted by interfering DVB-T/T2 transmitter, $P_{I\_DTTB\_permissible\_BS\_Rx}$, at LTE700 base station receiver is derived from

$$P_{I\_DTTB\_permissible\_BS\_Rx} = P_{DTTB\_e.i.r.p.\_Tx} - L_{Req\_path\_loss\_High\_Power}. \tag{5}$$

The maximum allowable interference level emitted by interfering DVB-T / DVB-T2, $P_{I\_DTTB\_High\_Power\_\max\ \_permissible\_BS\_Rx}$, at LTE700 base station receiver is

$$P_{I\_DTTB\_High\_Power\_\max\ \_permissible\_BS\_Rx} = 85.15\ dBm/8\ MHz \\ -206.65\ dB = -121\ [dBm]. \tag{6}$$

The calculated minimum protection distance (using ITU-R Recommendation P.1546-5), $d_{sep\_req\_DTTB\_High\_Power\_BS}$, between DVB-T/DVB-T2 transmitter and the victim receiving LTE700 base station is about 484 km (for T: 10 %; L: 50 %, at 30 m receiving antenna height).

The maximum allowable interference level emitted by interfering DVB-T/DVB-T2 transmitter, $P_{I\_DTTB\_Medium\_Power\_\max\ \_permissible\_BS\_Rx}$, at LTE700 base station receiver is

$$P_{I\_DTTB\_Medium\_Power\_\max\_permissible\_BS\_Rx} = 69.15\ dBm/8\ MHz$$
$$-190\ dB = -121\ [dBm]. \tag{7}$$

The calculated minimum protection (coupling) distance, $d_{sep\_req\_DTTB\_Medium\_Power\_BS}$, between DVB-T/DVB-T2 transmitter and the victim LTE700 base station receiver is about 298 km (for T: 10 %; L: 50 %, at 30 m receiving antenna height).

According to MCL calculations, the minimum separation distance needed between DVB-T/T2 and LTE BS receivers in the 694–790 MHz band to provide necessary performance of the LTE700 BS is 484 km (for High Power DTTB transmitter) and 298 km (for Medium Power DTTB transmitter).

B. Calculation Results of Coordination Trigger Field Strength Value Method Predetermined by GE06 Agreement

The protection of mobile service BSs against DTTB is defined in the GE06 Agreement, and the protected field strength value used in this paper complies with the GE06 Agreement. The ITU-R Recommendation P.1546-5 (using flat terrain) is used in this estimation. Calculation results are provided in Table 4.

Table 4. Calculation Results

Parameter	**Value**	
DTTB Tx/ BS Rx frequency	706 MHz (TV channel 57) / 708 MHz	
Transmitting DTTB station height	300 m (High Power), and 150 m (Medium Power)	
Receiving LTE BS height	30 m	
Coordination trigger field strength value predetermined by GE06 Agreement for protection of the mobile service base stations	14.6 dBµV/m at 20 m (or 18.3 dBµV/m at 30 m) in a 8 MHz reference bandwidth (BS corresponds to generic case, code NB) using ITU-R Recommendation P.1546-5 (T: 10 %; L: 50 %) [10]	
DTTB Tx power e.i.r.p.	85.15 dBm (High Power), and 69.15 dBm (Medium Power)	
DTTB system type	DVB-T/T2 High Power transmitter	DVB-T/T2 Medium Power transmitter
Calculated separation distance between DTTB Tx and LTE BS Rx	422 km	252 km

The calculation results present that the needed coupling distance between DVB-T/DVB-T2 and LTE700 base station receivers must be more than about 422 km for DVB-T/T2 High Power case and 252 km for DVB-T/T2 Medium Power case.

C. Monte Carlo Method Calculation Results

SEAMCAT simulation results demonstrate the required coupling distance between the DVB-T/T2 Tx and LTE BS Rx according to the protection criteria $I/N = -6\ dB$ defined for LTE BS receivers. In our study, the probability of interference *(PoI)* is assumed to be less than 5 % to ensure a sufficient protection level. For SEAMCAT simulations, 200 000 events are used. Results of Monte Carlo simulations are given in Table 5.

Table 5. Results of SEAMCAT Simulations

Separation distance between DVB-T/T2 Tx and LTE BS Rx, km	**Probability of interference (*PoI*), % for DVB-T/T2 High Power case**	**Separation distance between DVB-T/T2 Tx and LTE BS Rx, km**	**Probability of interference (*PoI*), % for DVB-T/T2 Medium Power case**
154	100.0	68	100.0
300	49.72	94	98.35
400	17.34	150	56.47
459	4.97	278	4.97
472	3.29	300	1.81

The simulation results demonstrate that the separation distance required has to be more than approximately 459 km regarding DVB-T/T2 High Power case and 278 km regarding DVB-T/T2 Medium Power case.

5. CONCLUSION

The paper has addressed a leading problem – coexistence requirements for the LTE and DVB-T/T2 deployment in the 700 MHz band in co-channel scenario between neighbouring countries.

Electromagnetic compatibility between DVB-T/T2 transmitter and LTE BS receivers has been estimated using three different methods: the MCL method, calculations of a coordination trigger field strength value predetermined by GE06 Agreement for single interferer scenario of DTTB station, and Monte Carlo simulations method using SEAMCAT.

According to MCL calculations, the minimum required separation distance between DVB-T/T2 and LTE BS receivers in the 694–790 MHz band to provide the necessary performance level of the LTE700 system is 484 km for High Power DTTB transmitter and 298 km for Medium Power DTTB transmitter.

According to the calculation results of coordination trigger field strength predetermined by GE06 Agreement, the required coupling distance is about 422 km for High Power DTTB transmitter and 252 km for Medium Power DTTB transmitter.

The SEAMCAT simulations demonstrate that the needed coupling distance has to be more than approximately 459 km regarding DVB-T/T2 High Power case and 278 km regarding DVB-T/T2 Medium Power case under condition that the probability of interference *(PoI)* less than 5 % is considered as a sufficient protection level.

The Monte Carlo method contributes to a more relaxed electromagnetic compatibility scenario in comparison with the MCL method. Applying different kinds of mitigation techniques, it is possible to improve electromagnetic compatibility of DVB-T/T2 and mobile service (LTE) systems used in neighbouring countries.

Since 5G NR non-AAS base station does not create more interference to other services in the same band or to adjacent band services than an LTE signal, the acquired results of this paper are also valid for 5G NR system.

These electromagnetic compatibility evaluation results can be used by National Regulatory Authorities (NRAs), mobile radiocommunication operators, equipment manufacturers and other involved parties when planning broadcasting and mobile service networks in the 700 MHz frequency band.

REFERENCES

1. Resolution 232 (WRC-12). (2012). *Use of the frequency band 694-790 MHz by the mobile, except aeronautical mobile, service in Region 1 and related studies*. Radio Regulations, Resolutions and Recommendations. International Telecommunication Union (ITU), Vol. 3.
2. Ancans, G., Bobrovs, V., & Ivanovs, G. (2013). Spectrum Usage in Mobile Broadband Communication Systems. *Latvian Journal of Physics and Technical Sciences*, *50* (3), 49–58.
3. Draft New Report ITU-R BT.[IMT_DTTB_694-790_Co-channel], Annex 9 to Joint Task Group 4-5-6-7 Chairman's Report, document 4-5-6-7/715-E. (2014). *Co-channel sharing and compatibility studies between digital terrestrial television broadcasting and international mobile telecommunication in the frequency band 694-790 MHz in the GE06 planning area*. International Telecommunication Union.
4. Ancans, G., Bobrovs, V., & Ivanovs, G. (2015). Frequency Arrangement for 700 MHz Band. *Latvian Journal of Physics and Technical Sciences*, *52* (1), 52–67.
5. Ancans, G., Stankevicius, E., & Bobrovs, V. (2015). Assessment of DVB-T Compatibility with LTE in Adjacent Channels in 700 MHz Band. *Elektronika ir Elektrotechnika*, *21* (4), 73–74.
6. ECC Report 297. (2019). *Analysis of the suitability and update of the regulatory technical conditions for 5G MFCN and AAS operation in the 900 MHz and 1800 MHz bands*. Electronic Communications Committee (ECC) within the European Conference of Postal and Telecommunications Administrations (CEPT).
7. Liaison Statement to Joint Task Group 4-5-6-7, Working Party 5D, Document 4-5-6-7/49-E. (2012). *Sharing Parameters for WRC-15 Agenda Item 1.2*. International Telecommunication Union.
8. Report ITU-R M.2292-0. (2013). *Characteristics of terrestrial IMT-Advanced systems for frequency sharing / interference analyses*. International Telecommunication Union.
9. Liaison Statement to Joint Task Group 4-5-6-7, Working Party 6A, Document 4-5-6-7/55. (2012). *Technical characteristics and other technical issues for terrestrial television broadcasting in connection with WRC-15 Agenda Item 1.2*. International Telecommunication Union.
10. CEPT Report 29. (2009). *Guideline on cross border coordination issues between mobile services in one country and broadcasting services in another country*. Electronic Communications Committee (ECC) within the European Conference of Postal and Telecommunications Administrations (CEPT).

LATVIAN JOURNAL OF PHYSICS
AND TECHNICAL SCIENCES
2020, N 5

DOI: 10.2478/lpts-2020-0026

NATURAL GAS METERING AND ITS ACCURACY IN THE SMART GAS SUPPLY SYSTEMS

J. Savickis[1], L. Zemite[2*], I. Bode[2], L. Jansons[2]

[1]ITERA Latvija
50 Skanstes Str., Riga, LV-1013, LATVIA
[2]Riga Technical University,
Faculty of Power and Electrical Engineering,
Institute of Power Engineering
12-1 Azenes Str., Riga, LV-1048, LATVIA
*e-mail: laila.zemite@rtu.lv

The successful implementation of smart metering in the European Union (hereinafter – EU) depends on criteria that are mostly determined by the Member States themselves. These criteria cover the regulatory framework and legislation necessary for the establishment and functioning of the smart metering system, the fulfilment of technical and commercial conditions, as well as the security of data collection, archiving and use. The introduction of the smart metering in different Member States has started at different times. In Latvia, its reference point was 2004, when the goal was set to maximise the use of telemetry in the natural gas metering. Currently, in the Latvian natural gas distribution system about 85 % of all consumption data are automatically processed.

One of the most important components of the smart natural gas metering is natural gas commercial metering devices (hereinafter – smart meters). They differ in both the principle and type of operation. Depending on the technology used, the metering range changes, and thus the accuracy of the measurements.

The article addresses some issues of further successful implementation of smart metering in the Latvian natural gas sector, as well as the measurement accuracy for smart natural gas meters.

Keywords: *Consumption data, distribution system, measurement accuracy, natural gas, natural gas flow, smart natural gas meters.*

1. INTRODUCTION

The natural gas smart metering cannot be implemented without a proper technical infrastructure, where one of the most important elements is smart natural gas meters themselves. They are rather different in both principle of operation and technological design. Depending on the technology used, the metering range and thus the accuracy of the measurements may differ.

By the end of 2020, the EU countries are expected to invest around 45 billion euro (hereinafter – EUR) in installation of around 45 million smart natural gas meters and almost 200 million smart electricity meters. At the same time, it is estimated that around 40 % of the natural gas consumers and 75 % of electricity consumers in the EU will be using smart electricity and gas metering devices in their household, businesses or public buildings. In most EU Member States, full replacement of mechanical electricity meters has already been implemented or is planned for the nearest future (3–5 years), but implementation of the smart natural gas metering in all segments of consumption is expected in just a few countries, for example, Italy and Finland [1].

Estimated costs of smart gas meters vary slightly across the EU as well, but on average the installation of such a device costs around 200–250 EUR per user and saves a total of 160 and 309 EUR, respectively, in the natural gas and electricity sectors. In terms of energy saving, smart metering can help to save up to 3 % of energy, which other would be wasted [2].

When the smart natural gas metering system is installed, the basic distribution costs consist of:

- one-time capital costs (including design, development and testing of the system);
- operating costs (including operation of the system and provision of data transmission, for example, with the usage of a SIM card and GSM communication).

Additionally, one-time capital and operating costs can be subdivided into the following expense categories:

- price of a smart meter;
- installation costs of a smart meter at the consumer's premises;
- communication system costs;
- IT system costs;
- system adaptation costs;
- maintenance and operating costs;
- data transmission costs;
- administrative expenses [3].

In Latvia, the Regulation of the Cabinet of Ministers No. 665 "Regulations on Metrological Requirements for Gas Consumption Meters and Volume Correctors" (hereinafter – Regulation No. 665) determines the minimum conditions for the natural gas flow, which apply to all types of natural gas meters, including the smart ones.

Table 1. The Natural Gas Flow Requirements

Class	Q_{max}/Q_{min}	Q_{max}/Q_t	Q_r/Q_{max}
1.5	≥ 150	≥ 10	1.2
1.0	≥ 20	≥ 5	1.2

According to Regulation No. 665, the term "minimum flow" (Q_{min}) means the flow at which the natural gas meter provides readings that meet the requirements for maximum permissible error (hereinafter – MPE), while the term “maximum flow” (Q_{max}) means the flow, at which the natural gas meter provides readings that meet the requirements for the MPE. The term “transient flow” (Q_t) is also used to refer to a flow between the maximum and minimum flow and at which the flow range is divided into two zones: the upper and the lower. Each zone has its own MPE. Additionally, the term “congestion flow” (Q_r) is applied to the highest flow at which the natural gas meter operates satisfactorily [4].

Regulation No. 665 also determines that MPE for the natural gas meters depends on their accuracy class. If a natural gas meter is intended to be used in the individual consumption sector, Class 1.5 shall be used for measurements, but if the $Q_{max / Qmin}$ ratio is equal to or greater than 150, Class 1.0 shall be used.

Table 2. Maximum Permissible Error Depending on the Accuracy Class of a Smart Gas Meter

Class	1.5	1.0
$Q_{min} \leq Q < Q_t$	3 %	2 %
$Q_t \leq Q \leq Q_{max}$	1.5 %	1 %

Figure 1 shows that different minimum and maximum flow measurement limits are allowed for different natural gas meters (including smart metering devices), and these limits are overlapping. In addition, there are other criteria that affect the accuracy of the natural gas metering (pressure losses, natural gas flow fluctuations, lower flow limits etc.) [4].

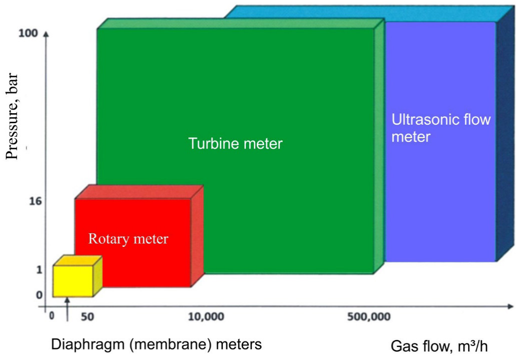

Fig. 1. Range of use of different natural gas meters.

In Latvia, the duration of the inspection period of the natural gas meters is set to be reasonable (5 years) and it protects the interests of the consumers; however, due to possible metering errors, the natural gas losses may increase. According to Paragraphs 26 and 27 of Decision No. 1/12 of the Council of the Public Utilities Commission of 6 August 2020 “Methodology for Calculating Natural Gas Distribution System Service Tariffs”, distribution system operation costs are calculated according to a formula that includes technological process provision and natural gas loss costs, as well as the forecasted natural gas consumption for technological needs. These additional requirements oblige the natural gas distribution system operator (hereinafter – SSO) to assess the future usefulness of the older diaphragm (membrane) natural gas meters in the household sector [5]. At the same time, the necessity of control measurements in apartment buildings should be evaluated in order to determine the difference between the actual consumption numbers and those declared by individual consumers.

2. CHARACTERISTICS OF SMART METERING AND USE OF DIFFERENT TYPES OF NATURAL GAS METERS

The introduction of smart metering in the EU Member States has started at different times. In comparison to smart electricity metering, the deployment of smart natural gas meters was and still is much slower. Although benefits of the smart metering system in the natural gas sector are obvious: it not only contributes to more efficient energy use, but also significantly optimises the management of the natural gas supply system and collection, analysis and archiving of data [6].

The smart meter communication system for data exchange consists of the following elements:

- a smart meter that performs the function of data registration and transmission;
- a data collector that receives and sends information from / to all meters connected to the system and installed in a particular area;
- communication systems (GSM, GPRS, etc.);
- information management systems [3].

Article 9 (2) of Directive 2012/27/EU provides that, when EU Member States implement smart metering and smart meters for natural gas and/or electricity consumption, in accordance with Directives 2009/72 / EC and 2009/73 / EC, they shall:

- ensure that the metering systems provide to final customers information on actual time of use and that the objectives of energy efficiency and benefits for final customers are fully taken into account when establishing the minimum functionalities of the meters and the obligations imposed on market participants;
- ensure the security of the smart meters and data communication, and the privacy of final customers, in compliance with relevant Union data protection and privacy legislation;
- require that appropriate advice and information be given to customers at the time of installation of smart meters, in particular about their full potential with regard to meter reading management and the monitoring of energy consumption [7].

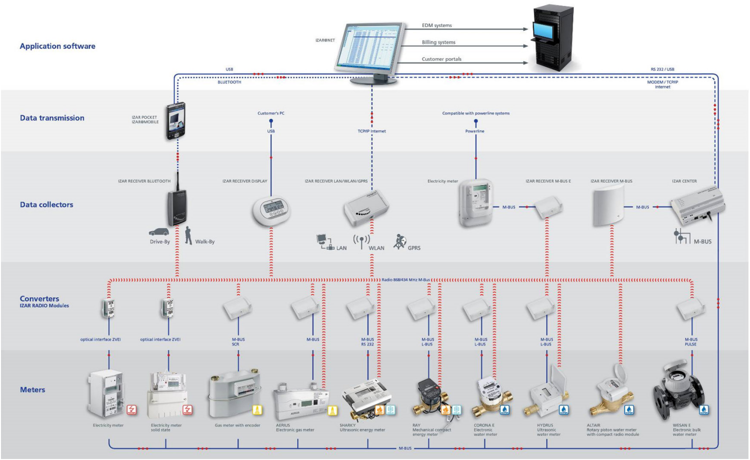

Fig. 2. The principal scheme of smart metering system
(smart meters, convertors, data collectors, data transmitters, and data processing software).

In absence of strict requirements for the choice of technical equipment and software, there is a situation where four data reading systems with different makeup and functionality coexist in the EU Member States, which at some extent hinders effective, comprehensive development of the smart natural gas metering. There are also no requirements set for external power supply to smart metering devices in high gas consumption facilities, where big amounts of data need to be read and transmitted several times a day.

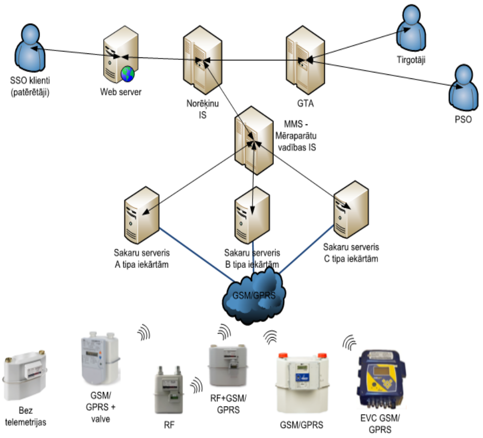

Fig. 3. Principle scheme of the natural gas smart metering system, JSC "Gaso".

For Latvia, a reference point for smart gas metering was 2004, when the goal was set to maximise the use of telemetry in the natural gas sector. Currently, in the Latvian natural gas distribution system about 85 % of all consumption data are automatically processed. Data transmission is carried out via GSM communication system by inserting a SIM card into the data transmission device. Around 3,100 pressure and temperature correctors have been installed in the Latvian natural gas supply system, of which 510 are equipped with telemetry. However, according to technical and functional parameters, uniform requirements for the smart meters for the natural gas in Latvia have not been determined yet. However, Section 16, Paragraph four of the Energy Efficiency Law (hereafter – EEL) allows the system operator, taking into account the needs and potential benefits of the energy consumers, to determine the minimum functions of a smart commercial metering device, including the possibility to obtain information on actual energy consumption in a specific period of time.

The EEL also stipulates that the system operator, when installing a smart commercial metering device, must provide energy consumers with information on the possibilities of the meter management and energy consumption monitoring [8]. The requirements for the protection of personal data in the EU derive from Regulation (EU) 2016/679 of the European Parliament and of the Council of 27 April 2016 on the protection of natural persons with regard to the processing of personal data and on the free movement of such data, and repealing Directive 95/46/EC (General Data Protection Regulation), which Latvia had enforced by the Personal Data Processing Law. The law, inter alia, provides that SSOs, as data controllers or processors, must also guarantee data security of the smart metering system and energy consumers [9].

Diaphragm (membrane) natural gas meters, which can also be equipped with a data transmission module, are mostly used for a low natural gas flow. In cases where natural gas has to be supplied to a small industrial enterprise or merchant, rotary natural gas meters are preferred. Turbine gas meters are designed to supply natural gas to industrial consumers at a massive, steady flow regime. However, under non-uniform load conditions, turbine meters generate metering errors [10]. Ideally, turbine meters should operate under stable and constant conditions of the natural gas flow in order to avoid pulsations and thus metering inaccuracies. If the flow of natural gas changes or is stopped altogether, the mechanism will continue to rotate for some time; thus, the metering inaccuracies are almost inevitable [11]. The effect of flow disturbances on the readings of the natural gas meter shall not exceed 1/3 of the maximum permissible error of metering instrument of a particular type and technological design.

Diaphragm natural gas meters are used in Latvia up to G25 level, because other types of the natural gas meters with a higher performance rate have rather large dimensions and lower accuracy. For example, at times of pulsation of turbine natural gas meters, the inertia of the turbine wheel and subsequent metering error may occur during on and off mode [12].

Ultrasonic and microthermal natural gas meters are an alternative to diaphragm, rotary and turbine natural gas meters. They are used when exclusively high measurement accuracy is required [13]. Microthermal meters can keep an accurate metering rate even at very low initial flows. If correct functioning of diaphragm natural gas meters largely depends on the temperature and pressure, which can be seriously jeopardized without temperature and pressure correction, microthermal meters adjust metering specification to these factors automatically [14]. In contrary to diaphragm natural gas meters, the membranes of which may lose their elasticity over time, microthermal meters do not have moving parts that are subject to wear and tear and can affect the accuracy of metering.

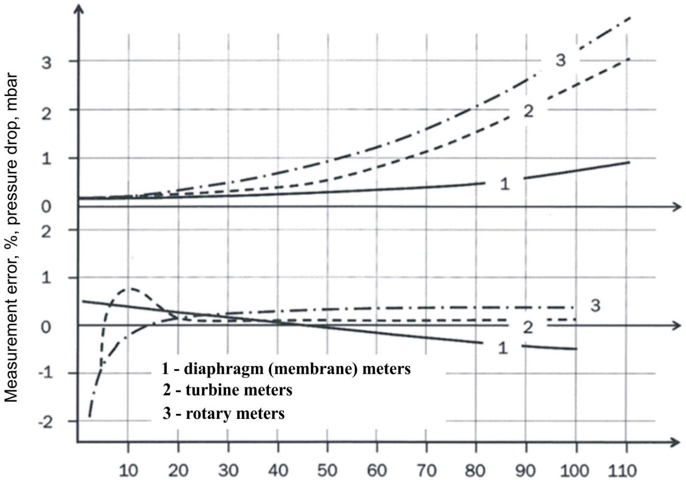

Fig. 4. Influence of pressure changes on metering errors of different type natural gas meters.

Studies have been carried out over the past decade in several European countries, including Italy, to determine the longevity of different types of the natural gas meters and variations in metering errors as the equipment ages and the degree of physical wear and tear increases.

One Italian study surveyed 402 diaphragm natural gas meters with different service life (up to 50 years old). As a result, it was concluded that the observed tendency of the natural gas metering deviation was in favour of gas consumers. At a minimum flow, the average metering error is close to zero or almost always with a negative tendency, maintaining an upward trend in favour of the gas consumer, as the service life of the meter increases [15].

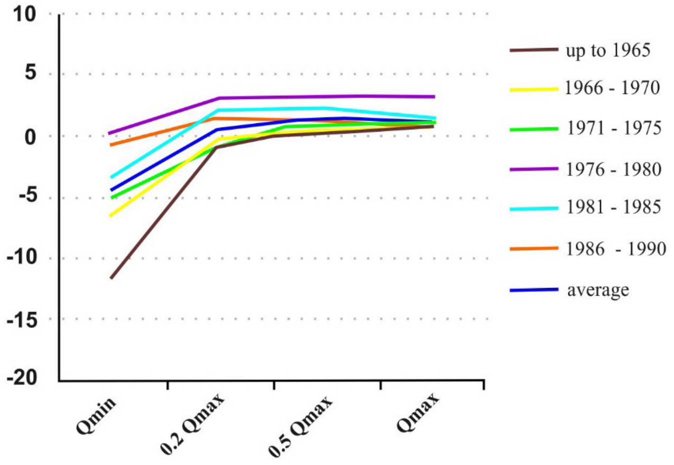

Fig. 5. The observed tendency of the natural gas metering deviation.

Another study, also from Italy, analysed dynamics of metering errors for diaphragm natural gas meters manufactured between 1965 and 2006. As a result of this study, it was confirmed that minimal metering errors appeared at a minimum flow, with a tendency to increase with age.

When comparing several types of smart natural gas meters according to the technical parameters of flow measurement, the best technical parameters refer to individual ultrasonic and microthermal meters with a wider measuring range, as well as the possibility to perform satisfactory at low minimum flows. However, external factors, such as installation location (outdoor or indoor), temperature, volumes of the gas flows, and other conditions may affect the technical parameters (operating temperature, battery life, etc.) or materials of the metering devices. Plastic parts of the meters wear out sooner at high flow volumes and pressure than metallic ones; thus, metallic parts can be manipulated externally – for instance, affected by magnets.

3. METERING ERRORS AND THEIR CORRECTION

The natural gas meter measures natural gas flow parameters under ideal conditions, but more precisely the amount of natural gas can only be determined at a certain temperature and pressure regime.

A temperature and pressure corrector that adjusts the metering data according to standard conditions (conditions at a natural gas pressure of 101,325 kPa and a temperature of 20 °C) can be used in three ways:

- determining the volume under certain standard conditions according to Charles' law;
- according to the ideal gas law, determining the volume at a certain standard temperature and pressure;
- on the basis of known real natural gas parameters, determining the volume under standard conditions.

The maximum permissible error of the natural gas meter increases as the conversion complexity grows, given that in the former case the operation is the simplest, and in the latter – the most complex [16]. Thus, a correction factor is determined that adjusts the listed natural gas volume. For example, if at a temperature of 18 °C the correction coefficient is 0.99308 and the measured volume of the natural gas is 1000 m^3, then the calculated volume will be 993.08 nm^3. On the other hand, as the temperature increases to 22 °C, the coefficient increases to 1.00692 and, accordingly, for the same measured volume, the calculated volume of the natural gas comes up to 1006.92 nm^3. Thus, a temperature change of 1 °C affects the measured volume by 0.346 % [17].

Meters with a built-in temperature compensating element would significantly reduce the possibility of metering errors. Such meters should also be used indoors, as the temperature and pressure at the location of the natural gas meter often differ from the standard temperature. For example, pressure, unlike standard conditions, can cause a meter mismatch of up to 1.97 % [17]. Problems with installation depth of the temperature sensor shell also might occur, and at a consumption of almost 8000 nm^3, the difference between the installation depth of the shell can cause losses of more than 500 EUR [17]. However, choosing a new ultrasonic or microthermal natural gas meter with the integrated communication module, temperature corrector and shut-off valve solves the problem of possible shell installation depth manipulations.

4. SMART METER USE AND ITS ADVANTAGES

The benefits of smart natural gas meters can be divided into several categories:

1. based on the technical parameters of equipment:
   - more accurate, dynamic and safe natural gas metering;
   - efficient management of a meter by receiving a system alarm signal (temperature, manipulation, battery, air in a pipe);
   - remote reading of a meter;
   - possibility to choose different communication solutions for data transfer (mobile, radio, optical cable or wireless technologies).
2. based on the efficient use in the natural gas systems:
   - remote automatic reading of data saves the system operator’s resources by reducing the need for physical inspection (reading, interruptions of the natural gas supply, verification of the physical condition of the equipment, etc.);
   - efficient and quick identification of the natural gas leaks or other technical problems in the gas pipelines [18];
   - reduction of unlawful natural gas use, with is easily identifiable by examining atypical loads, which do not correspond to the historical or most recent consumption profiles;
   - by fulfilling the obligations specified in Regulation of the Cabinet of Ministers No. 78 “Regulations on Trade and Use of Natural Gas” (hereinafter – Regulation No. 78), it is possible to improve system balancing forecast with more and more accurate consumption data [19];
   - improved customer service (applications, consumption data analysis, immediate consumption control and data reading);
   - the received data allows the operator to segment and profile customers according to their consumption specifications;

  - possibility to remotely and quickly cut off the supply of natural gas without entering the property. According to Regulation No. 78, DSO is entitled to suspend the supply of the natural gas in cases of non-settlement or termination of the supply agreement;
  - more convenient system management in case of major accident, crisis or state emergency, including fulfilment of the obligation of the system operator to restrict gas supply specified in Regulation of the Cabinet of Ministers No. 312 “Procedures for the Supply of Energy Users and the Sale of Fuel during the Energy Crisis and in the Event of a State Emergency”. Availability of more accurate data about the system allows for more accurate calculation of system losses in the above-mentioned cases, too [20];
  - installation of the smart metering system at gas metering checkpoints.
3. based on energy efficiency and comfort of the natural gas consumers:
  - convenient and accurate information about consumed natural gas, which can be obtained electronically;
  - permanent information on natural gas consumption allows consumers to re-examine their consumption habits and adjust them to save financial and energy resources.

5. CONCLUSIONS

Smart natural gas metering meets requirements for fast and accurate collection, analysis and archiving of the natural gas consumption data, as well as provides opportunities for SSOs to more effective evaluation and planning of the natural gas supply system development in various regions of Latvia and other EU countries. It also may contribute to the achievement of energy efficiency and system security targets [21]–[23], which ensure sustainable economic development and prevention of further climate change.

More attention should be paid to studies on usefulness of wider implementation of natural gas metering in Latvia. It is necessary to evaluate benefits that can be archived from different viewpoints, such as technical, economic, operational, administration, etc. Currently, neither in Latvia, nor in the EU as a whole, unified technical requirements for smart natural gas meters and guidelines for their operation have been developed and legally established, which to some extent hinders the overall pace of effective energy consumption. It is necessary to re-evaluate the link between smart metering of natural gas and variations in legal ownership of these meters in Latvia. It should be done to reduce bureaucratic and legal obstacles that prevent full implementation and use of smart natural gas metering.

Different types of the natural gas meters (including those that can be equipped with telemetry) have different minimum and maximum flow limits, and these limits overlap. In addition, accuracy of natural gas measuring may be affected by other factors, such as pressure losses and natural gas flow fluctuations.

When comparing several types of smart meters according to the technical parameters of flow measurement, the best results are demonstrated by individual ultrasonic and microthermal natural gas meters with a wider measuring range, as well as the possibility to enhance very low minimum flows.

Meters with a built-in temperature compensating element would significantly reduce the possibility of metering errors. Such meters should also be used indoors, as the temperature and pressure at the location of the natural gas meter often differ from the standard temperature.

The use of new ultrasonic or microthermal smart meters with the integrated communication module, temperature corrector and shut-off valve solves the problem of shell installation depth manipulations.

In Latvia, the duration of the meter inspection period is set to be reasonable and it protects the interests of consumers; however, due to metering errors, natural gas losses may increase between verification events. To avoid this situation in the individual consumption sector, it would be desirable to assess:

- future replacement of older diaphragm natural gas meters;
- opportunity to carry out more extensive inventory of the natural gas use in apartment buildings in order to pinpoint the difference between the actual and declared natural gas consumption;
- opportunity to replace multiple single unit (flat) natural gas meters with one single smart meter in apartment buildings as it is done in several EU countries, for example, Finland.

ACKNOWLEDGEMENTS

The research has been supported by the National Research Programme, project "Trends, Challenges and Solutions of Latvian Gas Infrastructure Development" (LAGAS) (No. VPP-EM-INFRA-2018/1-0003).

REFERENCES

1. Bianchini, A., Saccani, C., Guzzini, A., & Pellegrini, M. (2018). *Gas Smart Metering in Italy: State of the Art and Analysis of Potentials and Technical Issues*. [online]. [accessed 10 July 2020]. Available at https://www.researchgate.net/publication/330260200_Gas_smart_metering_in_Italy_state_of_the_art_and_analysis_of_potentials_and_technical_issues
2. Report from the Commission. *Benchmarking Smart Metering Deployment in the EU-27 with a Focus on Electricity* /* COM/ 2014/0356 final */ [online]. [accessed 1 September 2020]. Available at https://eur-lex.europa.eu/legal-content/GA/TXT/?uri=COM%3A2014%3A356%3AFIN
3. Eurogas Distribution Committee Report on Smart Gas Metering. (2010). [online]. [accessed 8 June 2020]. Available at http://www.eurogas.org/policy-areas/list-ofdocuments/?tx_ttnews%5Bcat%5D=9&tx_ttnews%5Bpointer%5D=2&cHash=700b097d2f12c3915436c9ec841ed8e2
4. Ministru kabineta noteikumi Nr. 665 "Noteikumi par metroloģiskajām prasībām gāzes patēriņa skaitītājiem un tilpuma korektoriem". [online]. [accessed 12 September 2020]. Available at: https://likumi.lv/ta/id/142374-noteikumi-par-metrologiskajam-prasibam-gazes-paterina-skaititajiem-un-tilpuma-korektoriem
5. Sabiedrisko pakalpojumu regulēšanas komisijas padomes lēmums Nr. 1/12

"Dabasgāzes sadales sistēmas pakalpojuma tarifu aprēķināšanas metodika". [online]. [accessed 17 August 2020]. Available at https://likumi.lv/ta/id/316609-dabasgazes-sadales-sistemas-pakalpojuma-tarifu-aprekinasanas-metodika

6. Toratti, J. (2020). *Appraising the economics of smart meters: Costs and benefits*. London: Routledge.
7. Directive 2012/27/EU of the European Parliament and of the Council of 25 October 2012 on energy efficiency, amending Directives 2009/125/EC and 2010/30/EU and repealing Directives 2004/8/EC and 2006/32/EC. [online]. [accessed 9 August 2020]. Available at https://eur-lex.europa.eu/legal-content/EN/TXT/?uri=celex%3A32012L0027
8. Energoefektivitātes likums (2016). [online]. [accessed 11 August 2020]. Available at https://likumi.lv/doc.php?id=280932
9. Fizisko personu datu apstrādes likums [online]. [accessed 6 June 2020]. Available at https://likumi.lv/ta/id/300099-fizisko-personu-datu-apstrades-likums
10. Stoltenkampa, P.W., Bergervoetb, J.T.M., Willemsa, J.F.H., van Uitterta, F.M.R., & Hirschberga, A. (2008). Response of Turbine Flow Meters to Acoustic Perturbations. *Journal of Sound and Vibration*, 258–278.
11. Cascetta, F., & Rotondo, G. (2015). Effects of Intermittent Flows on Turbine Gas Meters Accuracy. Second University of Naples, *Italy Measurement, 69*, 280–286.
12. Platais, I., & Graudiņš, P. (2008). *Gāzapgāde. 1.daļa. Ogļūdenražu deggāzes, to īpašības, metroloģija un sadedzināšana*. Rīga: RTU izdevniecība. 63. lpp.
13. Homann, K., Reimert, R., & Bernhard, K. (2013). *The gas engineer's dictionary. Supply infrastructure from A to Z.* Germany: DIV Deutscher Industrieverlag GmbH. 274 p.
14. AERIUS. (2018). *The Intelligent Form of Gas Metering*. [online]. [accessed 6 March 2020]. Available at http://www.diehl.com/fileadmin//diehl-metering/dlc/Gas/AERIUS_Folder_EN.pdf
15. Ficco, G. (2014). Metrological Performance of Diaphragm Gas Meteres in Distribution Networks – Flow Measurement and Instrumentation. *Flow Measurement and Instrumentation, 37*, 65–72.
16. Salkazanovs, J. (2015). *Dabasgāzes uzskaites datu attālināta nolasīšana*. Maģistra darbs. Rīga: Rīgas Tehniskā universitāte.
17. Bērzājs, M. (2017). *Dabasgāzes uzskaites optimizēšanas daudzdzīvokļu ēkās*. Maģistra darbs. Rīga: Rīgas Tehniskā universitāte. 44 lpp.
18. Zemite, L., Kutjuns, A., Bode, I., Kunickis, M., & Zeltins, N. (2018). Risk Treatment and System Recovery Analysis of Gas System of Gas and Electricity Network of Latvia. *Latvian Journal of Physics and Technical Sciences, 55* (5), 3–14. DOI: 10.2478/lpts-2018-0031.
19. Ministru kabineta noteikumi Nr. 78 "Dabasgāzes tirdzniecības un lietošanas noteikumi". [online]. [accessed 1 September 2020]. Available at https://likumi.lv/ta/id/289031-dabasgazes-tirdzniecibas-un-lietosanas-noteikumi
20. Ministru kabineta noteikumi Nr. 312 "Enerģijas lietotāju apgādes un kurināmā pārdošanas kārtība izsludinātas enerģētiskās krīzes laikā un valsts apdraudējuma gadījumā". [online]. [accessed 5 September 2020]. Available at https://likumi.lv/ta/id/229557-energijas-lietotaju-apgades-un-kurinama-pardosanas-kartiba-izsludinatas-energetiskas-krizes-laika-un-valsts-apdraudejuma-gadijuma
21. Zemite, L., Kutjuns, A., Bode, I., Kunickis, M., & Zeltins, N. (2018). Consistency Analysis and Data Consultation of Gas System of Gas-Electricity Network of Latvia. *Latvian Journal of Physics and Technical Sciences, 55* (1), 22–34. DOI: 10.2478/lpts-2018-0003.

22. Koposovs, A., Bode, I., Zemite, L., Dzelzitis, E., Odineca, T., Ansone, A., Selickis, A., ... & Jasevics, A. (2019). Optimization of the Selection Method for Reconstruction of Outworn Gas Distribution Pipeline. *Latvian Journal of Physics and Technical Sciences, 56* (5), 33–44. DOI: 10.2478/lpts-2019-0029.
23. Savickis, J., Zemite, L., Zeltins, N., Bode, I., & Jansons, L. (2020). Natural Gas and Biomethane in the European Road Transport: The Latvian Perspective. *Latvian Journal of Physics and Technical Sciences, 57* (3), 57–72. DOI: 10.2478/lpts-2020-0016.

LATVIAN JOURNAL OF PHYSICS
AND TECHNICAL SCIENCES
2020, N 5

DOI: 10.2478/lpts-2020-0027

THE EFFECTS OF NATURAL PAINT ON THE MOISTURE BUFFERING ABILITY OF PAPER PLASTER

N. Nutt*, A. Kubjas, L. Nei, A. Ruus

Tartu College, School of Engineering, Tallinn University of Technology
Puiestee 78, 51008 Tartu, ESTONIA
*e-mail: nele.nutt@taltech.ee

The scope of the Nordtest method is to evaluate the moisture buffer value (MBV) of materials exposed to indoor air. The test is intended to simulate daily variations with relative humidity (RH) between 75 % during 8 hours and 33 % during 16 hours.

The specimens follow a recipe that consists of waste paper, glue and water. Specimens made of paper plaster were covered with different colours.

The results of the experiment showed that the type of paint used and the number of layers applied affected the MBV. Natural colours have a better moisture permeability than chemical paints, but the number of natural colour layers affects the MBV. The higher the number of layers, the lower the MBV.

Keywords: *Buffer effect, building materials, humidity, indoor climate, moisture buffer value, material properties, moisture transport, Nordtest, natural paint, paper plaster, recycle, wastepaper.*

1. INTRODUCTION

In moderate to cold climates, people usually spend about 90 % of their time in enclosed spaces, so the indoor climate is a crucial factor of well-being [1]. The moisture buffering value (MBV) has been studied by several authors [2], [3], [4], [5]. The results of earlier laboratory studies about the interior plaster made of waste paper have shown that the MBV of paper plaster is excellent (MBV>2.0 = “excellent”) regardless of the type of paper [6], paper with clay [7], [8] or of the technology used to shred the paper [9].

The MBVs of waste paper of reusable materials [6] and MBVs of different clay plasters [10] have been studied. The effects of coating on the clay plaster hygroscopicity and water vapour permeability have also been researched [11]. However, the effects of coating on the hygroscopic abilities of paper plaster have not been studied.

Thickness of layer and water vapour transmission properties could be very different [12]. Water vapour transmission rate of casein paint and egg tempera (1-layer paint) were recorded as paints with "high" water vapour transmission rate (>150 g/(m^2d), while linseed oil paint acted as "medium" (15–150 g/(m^2d).

2. METHOD AND EQUIPMENT

To distinguish the moisture buffering abilities of plaster, the Nordtest method for determining the MBV of composite systems open to indoor climate was used [3]. The temperature was 23±0.5 °C throughout the experiment. Firstly, the specimens were kept in an environment with relative humidity (RH) at 50±5 % until an equilibrium (the change in the specimen mass is under 1 % during two weighings performed every 24 hours) was achieved. Then relative humidity was increased by 75 % for 8 hours and decreased by 33 % for 16 hours. The cycle was repeated until the average change in mass Δm (g) during three consecutive cycles was within 5 %.

The Nordtest protocol formula for $MBV_{practical}$ [g/(m^2·%RH)] calculations:

$$MVB_{8h} = \frac{m_{max} - m_{min}}{A\cdot(\varphi_{high} - \varphi_{low})}, \tag{1}$$

where $m_{min/max}$ is moisture mass (min and max) in the final sample (g or kg); A is exposed area (m^2); $\varphi_{high/low}$ is high/low RH (75–33) levels applied in the measurement.

According to the Nordtest method, specimens need to be weighed five times during one cycle [3]. We weighed specimens two times per cycle as the data from only two weighings were needed to calculate the MBV (Eq. (1)).

The equipment included the climate chamber RUMED 4101 affording RH 20...95 % with an accuracy of ±2–3 % and temperature of 0…60 °C with an accuracy of ±0.5 °C; Memmert Incubator Oven INB200 with temperature range from +30 °C (however, at least 5 °C above ambient) up to +70 °C and digital balance Kern PLT 1200-3A with an accuracy of 0.001 g. Climate chamber method was used at an environment temperature of 23±0.5 °C.

To evaluate the effect of moisture buffering to the room borders, daily hygroscopic inertia of the room [$I_{h,d}$, g/(m^3%RH)] defined by Ramos and others [13], [14] could be calculated:

$$I_{h,d} = \frac{\sum_i^n MBV_i \cdot S_i + \sum_j^m MBV_{obj}}{ach \cdot V \cdot t_g}, \tag{2}$$

where MBV_{obj}, MBV_i – moisture buffering value of objects and elements; S_i – the surface of an element i m^2; ach – air exchange rate h^{-1}; V – room volume m^3; t_g – vapour production period, h.

3. SPECIMENS AND COLOURS

The specimens were made according to the recipe that contains waste paper (newspaper paper), glue (methylcellulose produced by Henkel) and water. After drying the specimens were covered with paint.

Two different groups of specimens were made. The first group was used to study the effects of different paints on the MBV and the second group – to study the effects of different numbers of paint layers on the MBV.

The total number of specimens in the first group was 24 (3 x 8). Seven different colours were used to paint the specimens (casein primer, casein paint, tinted casein colour, linseed oil paint, egg oil tempera, clay paint and alkyd paint Akrit 7). The specimens were covered with two layers of paint (Fig. 1, Table 1).

Group 1 of specimens. Unpainted specimens.

Groups 2–4 of specimens. Casein paint is a natural interior colour with long traditions and is a suitable finish for natural plasters in a dry indoor environment. Casein colours enable water vapour to move through the plastered surfaces. All three casein colours (primer, white and tinted colour) were made of fat-free curd, borax (sodium tetraborate ($Na_2B_4O_7$)) and water. Casein primer is used to prime the surface. White casein paint is achieved by adding chalk (calcium carbonate ($CaCO_3$)) to the primer and different tones by adding coloured soils to the primer, which has been previously whitened by chalk.

Casein primer (Group 2 of specimens): 10g borax (sodium tetraborate ($Na_2B_4O_7$)) + 30ml water (temp 70 °C) + 250g curd (fat-free), promote casein hydrolysis + 1l water.

Casein paint (Group 3 of specimens): 10g borax + 30ml water (temp 70 °C) + 250g curd (fat-free), promote casein hydrolysis + 1l water + 400g chalk (calcium carbonate ($CaCO_3$)).

Tinted casein paint (Group 4 of specimens): 10g borax (sodium tetraborate ($Na_2B_4O_7$)) + 30ml water (temp 70 °C) + 250g curd (fat-free), promote casein hydrolysis + 1l water + 400g chalk (calcium carbonate ($CaCO_3$)) + yellow synthetic iron oxide (ferric oxide yellow) (Fe_2O_3).

Group 5 of specimens. Linseed oil paint is absorbed deep into the surface; hence, it has very permanent traits as it fills the pores on the surface and does not form a membrane on it. Linseed oil paint is used to cover wooden parts. Linseed oil produced by Kemet RV Ltd, which has a cold-pressed oil made of linseed as a binder, was used.

Group 6 of specimens. Egg oil tempera is a glaze paint, which has raw egg and linseed oil as binders, water as a dissolvent and pigments are added for tinting. Out of all the natural paints, egg oil tempera is one of the most washable and wearproof colours, which is also suitable to use in humid rooms. Suitable surfaces include wood and plastered surfaces. Egg oil tempera was made using equal parts (volume) of water, linseed oil (by Kemet RV Ltd) and raw eggs.

Group 7 of specimens. The surface of clay colour is rough; it has a lot of pores and does not tolerate mechanical stress. Clay paint can be used on all mineral and water-absorbing surfaces. Clay colour was made of clay finishing plaster by OÜ Saviukumaja. It consists of clay, sand (grain size 0-2 mm) and fibres of *Typha* stem. X-ray diffraction analysis was used to determine the mineralogical composition (% of mass) of the clay plaster mixture (< 0.2 mm): quartz 45.6, k-feldspar 6.6, plagioclase 7.9, chlorite 1.5, illite/illite-smectite 20.9, kaolinite 4.1, calcite 8.5, dolomite 4.0, hematite 0.5 and amphibole 0.5 wt% [15]. Clay paint was made by mixing 500 g of clay finishing plaster mixture (fraction 0.25) with 250 g of water.

Group 8 of specimens. Alkyd paint Akrit 7 is a water-based acrylate paint (produced by Eskaro Group AB Sweden) intended to be used indoors as a finishing product in dry rooms and rooms with elevated humidity.

Fig. 1. Examples of specimen groups:
1 – unpainted, 2 – casein primer, 3 – casein paint, 4 – tinted casein colour,
5 – linseed oil paint, 6 – egg oil tempera, 7 – clay colour,
8 – alkyd paint Akrit 7.

Table 1. Colours

Plaster group number	**Colour**	**No. of painted layers**	**Paper (g)**	**Glue (g) Glue/water**	**No. of samples**
1 control	Unpainted	0	500	20/1000	3
2	Casein primer	2	500	20/1000	3
3	Casein paint	2	500	20/1000	3
4	Tinted casein paint	2	500	20/1000	3
5	Linseed oil paint	2	500	20/1000	3
6	Egg oil tempera	2	500	20/1000	3
7	Clay paint	2	500	20/1000	3
8	Alkyd paint Akrit 7	2	500	20/1000	3

The second experiment focused on the effects of the natural colour thickness (number of layers) on the MBV. Two colours were used to paint the specimens: casein colour and clay colour. The total number of specimens was 60 (3 x 20). The specimens were covered with casein colour once, twice or, 5, 10, 15 and 20 times (Fig. 2, Table 2) and with clay colour once, twice, or 3, 4, 5, and 6 times (Fig. 3, Table 2). After each layer was painted, the specimens were left to dry. The experiment included the so-called control group, which consisted of unpainted specimens.

Fig. 2. Examples of specimen groups 2–7. Specimens covered with casein colour and the number of paint layers.

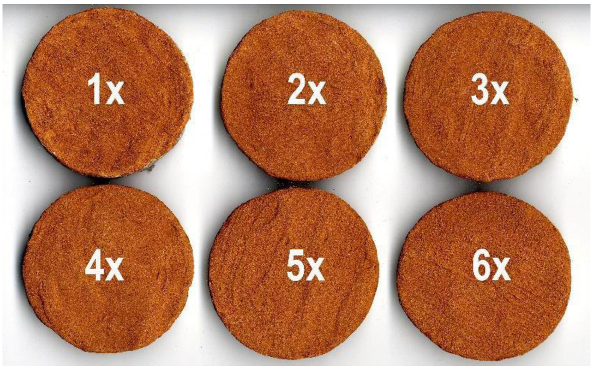

Fig. 3. Examples of specimen groups 8–13. Specimens covered with clay colour and the number of paint layers.

Table 2. Paint Layers

Plaster group number	**Colour**	**No. of paint layers**	**Paper (g)**	**Glue (g) Glue/water**	**No. of samples**
1 control	Unpainted	0	500	20/1000	3
2	Casein paint	1	500	20/1000	3
3	Casein paint	2	500	20/1000	3
4	Casein paint	5	500	20/1000	3
5	Casein paint	10	500	20/1000	3
6	Casein paint	15	500	20/1000	3
7	Casein paint	20	500	20/1000	3
8	Clay paint	1	500	20/1000	3
9	Clay paint	2	500	20/1000	3
10	Clay paint	3	500	20/1000	3
11	Clay paint	4	500	20/1000	3
12	Clay paint	5	500	20/1000	3
13	Clay paint	6	500	20/1000	3

4. RESULTS

Results achieved with the Nordtest method describe the moisture absorption and desorption of painted paper plaster surfaces and it is expressed with an index MBV. The change in relative moisture in actual living spaces is described by $\text{MBV}_{\text{practical}}$ [16]. As a result of changing relative humidity in cycles, the weight of the specimens also changed in cycles (see Fig. 4). According to the MBV [g/(m^2·%RH)@8/16h], materials can be classified as follows: negligible (0–0.2), limited (0.2–0.5), moderate (0.5–1.0), good (1.0–2.0), and excellent (2.0–) [10].

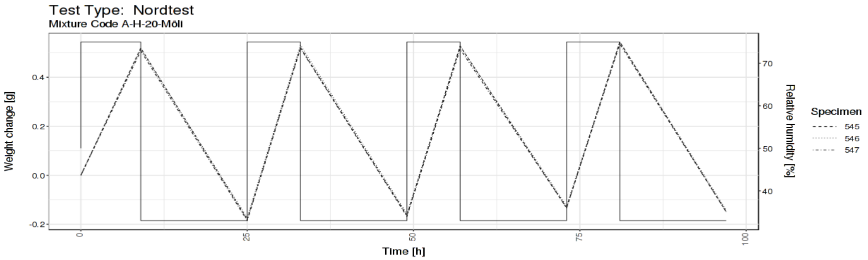

Source: Nele Nutt

Fig. 4. Changes in specimen weight (only weight change) in the final cycles (plaster group 7). The change in moisture cycles (RH 33 % and RH 75 %) in the climate chamber is portrayed by a solid line (Fig. 6, Table 4).

The results of the experiment with different colours showed that the MBV was highest (2.88 g/(m2·%RH)@8/16h) for unpainted paper plaster (plaster group 1). All the MBVs of paint covered specimens were lower (Fig. 5, Table 3). The MBVs of specimens that were covered with casein colour (plaster groups 2, 3, 4) and clay colour (plaster group 7) were a little lower than the unpainted paper plaster specimens.

Their MBV was higher than 2.0 [g/(m^2·%RH)@8/16h] (excellent). Specimens painted with egg oil tempera also had MBV higher than 2.0 [g/(m^2·%RH)@8/16h] (excellent). However, the MBV of specimens covered with linseed oil colour was smaller than 2.0 [g/(m^2·%RH)@8/16h] (good) and the specimens painted with alkyd paint Akrit 7 (plaster group 8) had MBV smaller than 1.0 [g/(m^2·%RH)@8/16h] (moderate) (Fig. 5, Table 3).

Table 3. MBV of Speciments

Plaster group number	**MBV [g/(m^2·%RH)@8/16h]**	**MBV classification**	**$I_{h,d}$, g/(m^3%RH)**
1	2.88	excellent*	0.51
4	2.70	excellent*	0.48
2	2.63	excellent*	0.47
7	2.61	excellent*	0.46
3	2.42	excellent*	0.43
6	2.34	excellent*	0.41
5	1.96	good*	0.35
8	0.59	moderate*	0.10

*negligible (0–0.2), limited (0.2–0.5), moderate (0.5–1.0), good (1.0–2.0), excellent (2.0–).

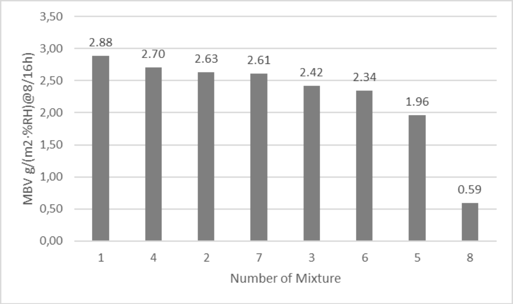

Fig. 5. MBV of specimens: 1 – unpainted, 2 – casein primer, 3 – casein paint, 4 – tinted casein colour, 5 – linseed oil colour, 6 – egg oil tempera, 7 – clay colour, 8 – alkyd paint Akrit 7.

The results of the experiment studying the effects of paint layers on the MBV showed that the more the layers, the lower the MBV (Fig. 6, Tabel 4).

Example: If we take a living room (walls) with measurements 5·4·2.6 m (windows and doors approx. 4 m^2), where ventilation rate according to energy efficiency requirements is 0.42 l/(sm^2), (air change 0.58 h^{-1} and time 8 hours), it is possible to calculate (Eq. (2)) the results of hygrothermal inertia index of the room (Tables 3 and 4).

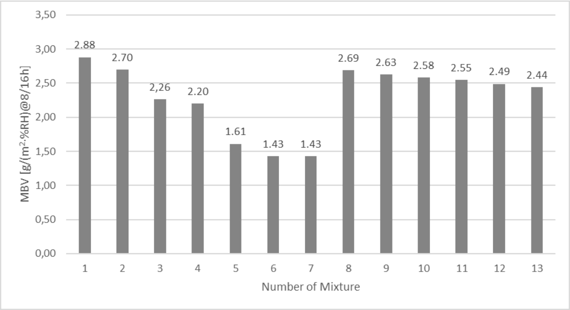

Fig. 6. MBV of mixtures: 1 – unpainted, 2–7 casein paint, 8–13 clay paint.

Table 4. MBV of Mixtures

Plaster group number	**No. of paint layers**	**MBV [g/(m^2·%RH)@8/16h]**	**MBV classification**	**$I_{h,d}$, g/(m^3%RH)**
1 control	0	2.88	excellent*	0.51
2	1	2.70	excellent*	0.48
3	2	2.26	excellent*	0.40
4	5	2.20	excellent*	0.39
5	10	1.61	good*	0.28
6	15	1.43	good*	0.25
7	20	1.43	good*	0.25
8	1	2.69	excellent*	0.48
9	2	2.63	excellent*	0.47
10	3	2.58	excellent*	0.46
11	4	2.55	excellent*	0.45
12	5	2.49	excellent*	0.44
13	6	2.44	excellent*	0.43

*negligible (0–0.2), limited (0.2–0.5), moderate (0.5–1.0) good (1.0–2.0), excellent (2.0–).

5. CONCLUSION AND DISCUSSION

Our experiment showed that:

- The MBV of paper plaster was affected when covered with paint. Unpainted paper plaster had the MBV of 2.88 g/(m^2·%RH)@8/16h. All the MBVs of paint covered paper plasters were under 2.70 g/(m^2·%RH)@8/16h.
- Colours had a different impact on the MBV of paper plaster. Out of all the natural colours, casein and clay colours inhibited the MBV the least. Their MBVs stayed within 2.70–2.42 g/(m^2·%RH)@8/16h.
- MBVs of all casein colours (casein primer, casein paint, tinted casein colour) were different from each other but stayed between 2.70 and 2.42 g/(m^2·%RH)@8/16h. Tinted casein colour had the highest MBV of 2.70 g/(m^2·%RH)@8/16h. It was followed by casein primer with MBV of 2.63 g/(m^2·%RH)@8/16h and casein paint with MBV of 2.42 g/(m^2·%RH)@8/16h.
- MBV of paper plaster decreased significantly as the number of casein colour layers increased. MBV was 2.70 g/(m^2·%RH)@8/16h with one layer of colour, 2.20 after 10 layers and 1.43 g/(m^2·%RH)@8/16h after 20 layers had been applied.
- From the colours containing oil, linseed oil paint was the one that inhibited the MBV of paper plaster and it was 2.61 g/(m^2·%RH)@8/16h.
- MBV of egg oil tempera covered paper plaster was the lowest at 0.59 g/(m^2·%RH)@8/16h.
- The effect of clay colour on the MBV was notable. When the MBV of unpainted paper plaster was 2.88 g/(m^2·%RH)@8/16h, then the MBV of clay colour covered specimens was 2.63 g/(m^2·%RH)@8/16h.
- The number of layers (1–6) was influential for clay colour covered specimen. The MBV decreased with each added layer of clay colour. When the MBV of paper plaster with one layer of colour was 2.69 g/(m^2·%RH)@8/16h, then after six layers the MBV was 2.44 g/(m^2·%RH)@8/16h.

Literature states [17] that casein colour does not inhibit the movement of water vapour through the plaster surface. However, our experiment showed that the MBV depended, firstly, on the composition of casein colour and, secondly, on the number of paint layers.

If a pigment is added to tone white casein colour, which is made with chalk, then the MBV is affected. At the same time, it should be taken into consideration that different pigments have a different chemical composition; thus, they can have both positive and negative effects on the MBV. It is necessary to study how different pigments affect the MBV of a tinted casein colour. This, in particular, is important as the chemical reactions between paper plaster (cellulose) and paint may affect the MBV. Also when making paper plaster, the cellulose hydrogen (H) is replaced by methyl (CH_3) radicals; hence, the possibility to form hydrogen bonds decreases.

Priming wall surfaces is a common method used to decrease painting costs. Primers are cheap because they have no pigment. Casein primer is intended to be used on walls with casein paint. Our experiment showed that the MBV was higher for the wall surface covered with casein primer than with only casein paint. Therefore, we recommend using casein primer as the first layer when painting paper plaster with casein colours. In the future, the effects of different combinations of casein primer and casein paints on the MBV should be studied.

It cannot unequivocally be said that casein colour enables the water vapour to move through surfaces as the previously mentioned literature states because the MBV of paper plastered surfaces decreases when the walls are repeatedly covered with casein colour (whitened during renovation). As new casein paint is directly added on top of the old casein colour layer, it should be taken into consideration that continuously adding paint layers will decrease the MBV of the wall surface.

Applying paper plaster does not require specific skills on the contrary to the application of clay plaster, and, therefore, it is executable by anyone. If the intent is to achieve a wall that replicates clay plaster, a good solution is to paint paper plastered walls with clay colour. However, it should be considered that each added layer of clay colour decreases the MBV of that wall. The same effect occurs when painting with casein paint.

Linseed oil and egg oil tempera both contain linseed oil. Linseed oil is absorbed deep into the surface and fills the pores; thus, the paper plaster covered with linseed oil has a lower MBV than the one covered with egg oil tempera. However, egg oil tempera is wearproof and washable and also suitable for humid spaces.

Calculation of daily hygroscopic inertia gives us information about the influence of MBV on the room together with ventilation and service area. Sample calculation was made for a case when ventilation is according to energy performance requirements [0.42 l(/sm^2)] and the whole wall area is acting. By using this calculation, everybody can find a suitable solution for different materials, ventilation rates, service areas and time to reduce peaks of RH variation.

Our experiments showed that the MBV of paper plastered and painted wall surfaces depended on the chosen colour and the number of applied layers of that colour. Further research should entail the study of other hygroscopic abilities of painted paper plaster. In addition to the MBV and the densities of materials studied in the research, the behaviour of other parameters should also be examined. Further research should also start to observe other moisture properties. The method described in the standard "EVS-EN ISO 12571:2013 Hygrothermal performance of building materials and products – Determination of hygroscopic sorption properties" [18] is used to study the sorption of water vapour when determining the hygroscopicity of porous materials. To study the conductivity of water vapour, the method from "EVS-EN ISO 12572:2016 Hygrothermal performance of building materials and products – Determination of water vapour transmission properties – Cup method" [19] was used.

ACKNOWLEDGEMENTS

This study has been supported by Tartu College of Tallinn University of Technology. The authors would like to thank Kadri Mets for improving English of the manuscript.

REFERENCES

1. Minke, G. (2006). *Building with earth: Design and technology of a sustainable architecture*. Basel: Birkhäuser.
2. Mazhoud, B., Collet, F., Pretot, S., & Chamoin, J. (2016). Hygric and Thermal Properties of Hemp-Lime Plasters. *Build*

Environment, *96*, 206–216.

3. Rode, C. (2005). *Moisture buffering of building materials.* BYG DTU126 Report. Department of Civil Engineering, Technical University of Denmark, Kongens Lyngby.
4. Svennberg, K. (2006). *Moisture Buffering in the Indoor Environment*. PhD Thesis. Lund: Lund University.
5. Zhang, M., Qin, M., & Chen, Z. (2017). Moisture Buffer Effect and Its Impact on Indoor Environment. *Procedia Engineering*, *205*, 1123–1129. DOI: 10.1016/j.proeng.2017.10.417
6. Teearu, M.-L. (2018). *Paberkrohvi niiskustehniliste omaduste määramine: sorptsioon, veeauru läbilaskvus ning niiskuspuhverdusvõime* [Determinantion of Hygrothermal Performance of Paper Clay: Sorption, Water Vapour Permeability and Moisture Buffering]. Master's Thesis. Tallinn: Tallinn University of Technology. (In Estonian)
7. Nutt, N., Kubjas, A., & Nei, L. (2020). Adding Waste Paper to Clay Plaster to Raise Its Ability to Buffer Moisture. *Proceedings of the Estonian Academy of Sciences*, *69* (3), 179–185. DOI: 10.3176/proc.2020.3.01
8. Nutt, N., & Kubjas, A. (2020). Moisture Buffer Value of Composite Material Made of Clay-Sand Plaster and Wastepaper. *Journal of Sustainable Architecture and Civil Engineering*, *2* (26).
9. Soolepp, M., Ruus, A., Nutt, N., Raamets, J., & Kubjas, A. (2020). Hygrothermal performance of paper plaster: influence of different types of paper and production methods on moisture buffering. *E3S Web Conf., 172*. 2020 12th Nordic Symposium on Building Physics (NSB 2020) https://doi.org/10.1051/e3sconf/202017214010
10. Vares, O., Ruus, A., Raamets, J., & Tungel, E. (2017). Determination of Hygrothermal Performance of Clay Sand Plaster: Influence of Covering on Sorption and Water Vapour Permeability. *Energy Procedia*, *132*, 267–272. DOI: 10.1016/j.egypro.2017.09.719
11. Soosaar, H. (2017). *Pinnakatte mõju savikrohvi hügroskoopsusele ja veeauru läbilaskvusele* [Influence of Finishing on Clay Plaster Hygroscopicity and Water Vapour Permeability]. Master's Thesis. Tallinn: Tallinn University of Technology. (In Estonian)
12. Ruus, A., Peetsalu, P., Tohvri, E., Lepasaar, T., Kirtsi, K., Muoni, H. … & Kabanen, T. (2011). Water Vapour Transmission Properties of Natural Paints. *Agronomy Research*, *9* (Biosystem Engineering Special Issue 1), 197–201.
13. Ramos, N.M.M., & Freitas, V.P. (2008). Laboratory testing for daily hygroscopic inertia assessment. In 8th Symposium on Building Physics in the Nordic Countries, 16–18 June 2008 (pp. 809–916). Copenhagen, Denmark: Technical University of Denmark.
14. Ramos, N. M. M., Delgado, J. M. P. Q. & Freitas, V. P. (2010). Influence of Finishing Coatings on Hygroscopic Moisture Buffering in Building Elements. *Construction and Building Materials*, *24*, 2590–2597.
15. Altmäe, E., Ruus, A., Raamets, J., & Tungel, E. (2019). Determination of Clay-Sand Plaster Hygrothermal Performance: Influence of Different Types of Clays on Sorption and Water Vapour Permeability. In *the 9th International Cold Climate Conference: Sustainable New and Renovated Buildings in Cold Climates*, 12–15 March 2018 (pp. 945−955). Kiruna, Sweden: Lund University. DOI: 10.1007/978-3-030-00662-4_80
16. Janssen, H., & Roels, S. (2009). Qualitative and Quantitative Assessment of Interior Moisture Buffering by Enclosures. *Energy and Buildings*, *41* (4), 382–394. DOI: 10.1016/j.enbuild.2008.11.007
17. Pere, R., & Elvisto, T. (2009). *Looduslikud värvid ehituses [Natural paints in construction]* Tallinn: Ajakirjade kirjastus. (In Estonian)
18. EVS-EN ISO 12571:2013 Hygrothermal performance of building materials and products – Determination of hygroscopic sorption properties.
19. EVS-EN ISO 12572:2016 Hygrothermal performance of building materials and products – Determination of water vapour transmission properties – Cup method.

LATVIAN JOURNAL OF PHYSICS
AND TECHNICAL SCIENCES
2020, N 5

DOI: 10.2478/lpts-2020-0028

THE COMPARISON OF THE EFFICIENCY OF SMALL WIND TURBINE GENERATORS WITH HORIZONTAL AND VERTICAL AXIS UNDER LOW WIND CONDITIONS

D. Bezrukovs[1], V. Bezrukovs[1]*, Vl. Bezrukovs[1],
M. Konuhova[1], S. Aniskevich[2]

[1]Engineering Research Institute
"Ventspils International Radio Astronomy Centre",
Ventspils University of Applied Sciences,
101 Inzenieru Str., Ventspils, LV-3601, LATVIA
[2]Latvian Environment, Geology and Meteorology Centre
165 Maskavas Str., Riga, LV-1019, LATVIA
*e-mail: elmag@inbox.lv

The authors perform a comparative analysis of the efficiency of two types of low-power wind energy conversion systems with horizontal and vertical axis in the meteorological conditions of Latvia. The analysis is based on long-term wind speed measurements over the period of two years conducted by a network of 22 observation stations at the height of 10 *m* above the ground. The study shows that in the conditions of Latvia wind turbines with a horizontal axis are expected to work with greater efficiency than similar installations with a vertical axis. The paper presents the models of the spatial distribution of average wind speed, Weibull wind speed frequency distribution parameters and the values of the expected operational efficiency for small wind turbine generators. The modelling results are presented in the form of colour contour maps. Overall, the results of the study can serve as a tool for forecasting annual energy production and for estimating the feasibility of commercial use of wind energy at the height of 10 *m* in the territory of Latvia.

Keywords: *Annual Energy Production, map, Small Wind Turbine Generator, wind energy, wind speed at the height of 10 m.*

1. INTRODUCTION

Due to the lack of significant reserves of fossil fuels in Latvia, the national economy considerably relies on energy import. The dependence of the country's economy on external supplies leads to the fact that the state is interested in supporting power stations using locally available natural resources and renewable energy sources [1]–[6].

Wind currents reaching the Latvian territory from the direction of the Baltic Sea represent a source of renewable energy, which can be used to produce electricity on an industrial scale. Therefore, studies aimed at estimating the expected efficiency of wind energy conversion systems (WECS) depending on their location in the territory of the country are highly relevant.

There is a number of publications devoted to the evaluation of the potential and the distribution of the wind energy resource in the territory of Latvia [7], [8]. However, modern meteorological equipment performing physical wind speed measurements simultaneously in different regions of the country provides a more reliable basis for estimating average wind speed and the spatial distribution of wind energy potential over the land surface.

The authors of the current study perform an assessment of the expected efficiency of low-power wind generators in the wind conditions typical of Latvia. A distinctive feature of these generators is that they transform the energy that wind carries at an altitude of 10–20 *m* above the ground surface. In most cases, a Small Wind Turbine Generator (SWTG) is used to power an autonomous load or serve as a backup power source at rural installations, the operation of which does not entirely depend on the power grid connection. Forecasting the efficiency of work and determining the Annual Energy Production (AEP) of the SWTG can be done only on the basis of long-term measurements of wind speed. However, the need to perform these measurements and calculate the AEP creates a problem for small households. Therefore, the authors of this study propose to use historical records of long-term measurements of wind speeds that are available in the archive of the national meteorological observation service for forecasting the efficiency of low-power wind generators.

The study is based on wind speed measurements over the period of two years from 1 January 2015 to 31 December 2016 [9]. All wind speed measurements were performed with 1 min increments at the height of 10 *m* above the ground using certified measuring sensors installed at 22 stations of the National Hydrometeorological and Climatological Service of the Latvian Environment, Geology and Meteorology Center (LEGMC).

Based on the available wind speed measurements, data specific indicators of wind energy that characterise the wind flow in this region are derived and an estimation of the average (AEP) for potential wind power plants is performed [10], [11].

The study of the SWTG performance is based on the power curves of two types of SWTG: Horizontal Axis Wind Turbines (HAWT) with rated power of 0.75, 2.5, 5.0, 20.0 *kW* and Vertical Axis Wind Turbines (VAWT) with 0.75, 2.5, 6.0 *kW*.

Based on the results of wind speed measurements and the estimation of the SWTG performance in the territory of Latvia, the models of the spatial distribution of averaged wind speed and wind energy density in the form of colour contour maps with a 1x1 km resolution were created. The contour maps identify the areas beyond which the measured values change with a certain step.

The developed models of the spatial distribution of the value of capacity factor characterising the effectiveness of the SWTG can serve as a convenient tool and reference material for analysing the feasibility of the SWTG application in various regions of Latvia. The obtained results allow estimating the prospects of commercial use of wind energy at the height of 10 *m*.

The rest of the paper is structured as follows: Section 2 provides the model of the spatial distribution of wind energy resource in Latvia. Section 3 presents the power curves of the selected SWTG. Section 4 is devoted to spatial distribution modelling of the efficiency of SWTG in Latvia. Section 5 provides the summary of the results, discusses their implications and makes conclusions on the prospects of estimating the SWTG efficiency at the height of 10 *m* above the ground.

2. THE SPATIAL DISTRIBUTION OF WIND ENERGY RESOURCE

Due to the cyclical nature of wind flows and nonlinear relationship between wind speed and energy it carries, wind energy potential assessment that takes into consideration only average wind speed values can be misleading.

The estimation of the average wind speed value for the period of measurements from 1 January 2015 to 31 December 2016 at each measurement site is performed in line with Eq. 1:

$$V_{avg} = \frac{1}{n}\sum_{i=1}^{n} V_i \,, \qquad (1)$$

where V_i – average wind speed with 1 *min* increments, *m/s*; n – the number of measurements for the entire period; i – the number of a measurement interval 1, 2, 3 … *n*.

The value of the average energy density that the air flow carries over an area of 1 m^2 is calculated from Eq. 2 [12]:

$$P_{avg} = \frac{1}{2}\rho V_{avg.cub}^{3} \,, \qquad (2)$$

where ρ – air density (*1.23 kg/m³* for standard condition at the sea level and temperature *15 °C*); $V_{avg.cub}^3$ – average cubic wind speed, *m/s*.

Average cubic wind speed can be calculated based on actual wind speed measurements according to Eq. 3:

$$V_{avg.cub} = \sqrt[3]{\frac{1}{n}\sum_{i=1}^{n} V_i^3} \,, \qquad (3)$$

where V_i – average wind speed for 1 *min* measurement interval, *m/s*; *n* – the number of measurements for the entire measurement period; *i* – the number of a measurement interval 1, 2, 3 … n.

As can be inferred from Eq. (2), the amount of energy carried by the wind is proportional to the value of the average cubic wind speed (see Eq. 3). At the same time, the classification of the territory of Latvia into five categories according to the level of the average cubic wind speed makes it is possible to estimate the potential of the wind energy resource available in these regions.

Assuming that the maximum value of the average energy density, which the wind carries on the shore of the Baltic Sea, is taken as 1.0, then the values of the average energy density in relative units for each station will be determined by Eq. 4:

$$P'_{avg.i} = V^3_{avg.cub.i} \Big/ V^3_{avg.cub.\max}, \qquad (4)$$

where $V^3_{avg.cub.\max}$ – average cubic wind speed at Ventspils station situated on the shore of the Baltic Sea; $V^3_{avg.cub.i}$ – average cubic velocity at each of the 22 stations; i – observation station 1, 2, 3 … 22.

By interpolating the obtained values, it is possible to create a map of the spatial distribution of the average density of wind energy $P'_{avg.i}$ in the territory of Latvia in relative units, which is shown in Fig. 1.

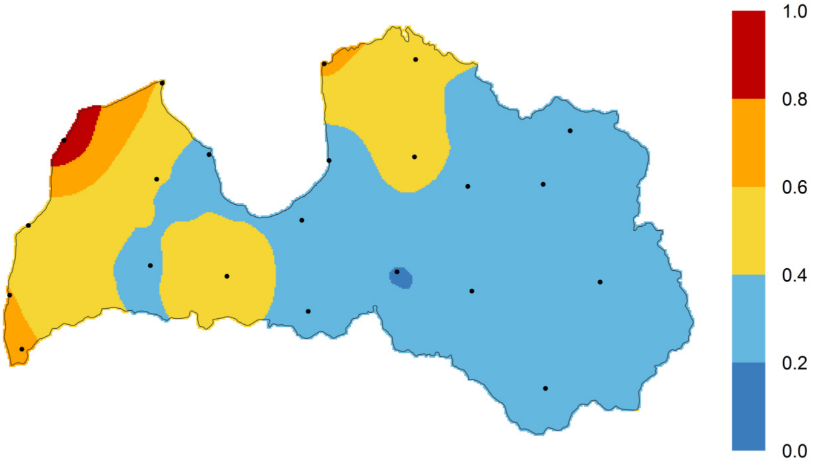

Fig. 1. Model of the spatial distribution of the average wind energy density in relative units P'_{avg} at the height of 10 *m* above the ground in the territory of Latvia.

Based on the model of the spatial distribution of the average wind energy density in Fig. 1, it is possible to identify regions, where SWTG with mast height of 10–20 *m* would have the highest efficiency.

3. POWER CURVE OF SWTG

Based on the results of wind speed analysis, it is possible to make a forecast with respect to the SWTG performance in the territory of Latvia. The current study considers two types of WECS: HWAT with rated power of 0.75, 2.5, 5.0, 20.0 *kW* and VAWT with 0.75, 2.5, 6.0 *kW*, which can operate at the height of 10 *m*. The two types of generators are shown in Figs. 2 and 3, respectively.

Fig. 2. Horizontal Axis Wind Turbine (HAWT) 0.75 *kW*.

Fig. 3. Vertical Axis Wind Turbine (VAWT) Darrieus H-type 0.75 *kW*.

The main technical and design characteristics of the SWTG are summarised in Table 1. The provided information is in line with the models presented in the Catalogue of the European Urban Wind Turbine Manufacturers [13].

Table 1. Technical Characteristics of HAWT and VAWT Darrieus H-Type SWTG with Rated Power of 0.75, 2.5, 5.0, 20.0 *kW* and 0.75, 2.5, 6.0 *kW*

Turbine type	**Rated power, *kW***	**Rotor height, *m***	**Rotor diameter, *m***	**Rated wind speed, *m/s***
VAWT	0.75	1.50	1.50	14.0
	2.50	2.88	1.99	14.0
	6.0	5.00	3.30	14.0
HAWT	0.75	–	2.40	12.0
	2.50		5.00	11.0
	5.0		5.40	11.0
	20.0		8.00	12.5

The efficiency of a WECS depends on the aerodynamic properties of the wind turbine and the wind type prevailing in the region. Therefore, it is of interest to evaluate the advantages of using both convector types in the specific conditions of the Latvian landscape. For comparison, Fig. 4 shows the power curves of HAWT 0.75, 2.5 *kW* and VAWT 0.75, 2.5 *kW*.

From the analysis of the power curves, it follows that a distinctive feature of HAWT generators is a steep power curve leading to a higher starting torque. At the same time, as it can be seen from Table 1 and Fig. 4, the rated wind speed for VAWT type generators reaches 14 *m/s*, while for HAWT the rated speed is 11–12.5 *m/s*. It means that the operating range of the considered VAWT type generators is between 3 and 14 *m/s* while for HAWT type generators it is between 2 and 11–12.5 *m/s*.

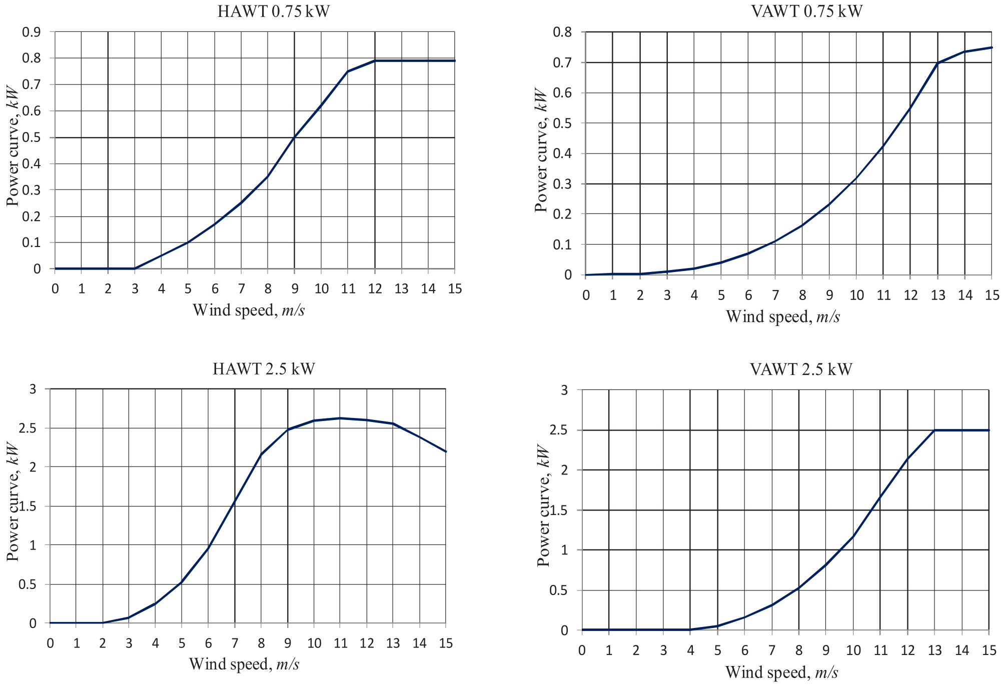

Fig. 4. Power curves P(V) of HAWT 0.75, 2.5 *kW* and VAWT 0.75, 2.5 *kW* Darrieus H-type.

4. MODELLING THE EFFICIENCY OF SWTG

The nature of the wind is characterised by cyclic changes in the flow speed and the duration of its gusts. On top of it, in various regions, wind fluctuations have characteristic features that are determined by the landscape and geographic proximity to the sea.

The study of wind properties is typically based on the analysis of wind speed measurement results obtained over a long period of time [14]. Methodological approach foresees grouping the measurement results into bins, which correspond to the selected speed intervals with a certain step. For each bin, the total recurrence time of this rate is determined, which can be expressed as a percentage of the total measurement time.

For the analysis of wind speed distribution, the most often used approximation is Weibull probability density function. This function is considered to be a good approximation of the wind speed frequency distribution and is described as follows:

$$F(V) = \frac{k}{c}\left(\frac{V}{c}\right)^{k-1} \exp\left[-\left(\frac{V}{c}\right)^{k}\right] \quad \text{for } V > 0 \ , \tag{5}$$

where c – scale factor; k – shape factor; V – wind speed, *m/s*.

Parameters of the Weibull wind speed frequency distribution functions were estimated using the Maximum Likelihood Method for 22 stations [15]. The maximum likelihood estimator is found by maximising the likelihood function and was calculated using functions from the package MASS of R language [16].

Once the distribution parameters are estimated, it is necessary to perform a goodness of fit test, which checks the conformity between observations and theoretical distribution. This is done by applying the Kolmogorov-Smirnov test, which measures the maximum distance between the empirical and the fitted distribution functions.

The hypothesis that the two distributions are equal is rejected if the distance exceeds a certain critical value [15]. Following the estimation of the parameters of the fitted distribution, it is necessary to assess critical values by applying the bootstrap procedure [17]. Hypothesis was not rejected for any of the stations at 5 % significance level, thus confirming the applicability of the Weibull distribution for the average wind speed data.

The way, how properties of the wind flow differ across various regions of the country can be represented in the form of a spatial distribution map of Weibull distribution function parameters, as shown in Figs. 5 and 6. The Weibull distribution parameter values depend on regional topography and site proximity to the Baltic Sea and the Gulf of Riga.

The scale parameter values *c* (Fig. 5), which stretch or shrink the distribution, are decreasing with the distance from the sea, indicating that coastal stations have wider probability density functions. The spatial distribution of the shape parameter values *k* (Fig. 6) is influenced by topography as the lowest values are observed in the highlands. Overall, the shape parameter *k* values vary from 1.6 to 2.1, indicating that the density function has a positively skewed bell shape.

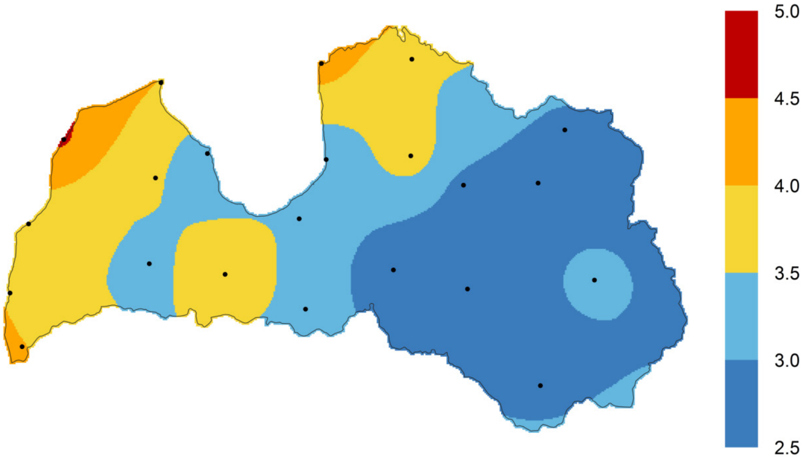

Fig. 5. Model of the spatial distribution values of the scale parameter *c* of Weibull wind speed probability density at the height of 10 *m* above the ground.

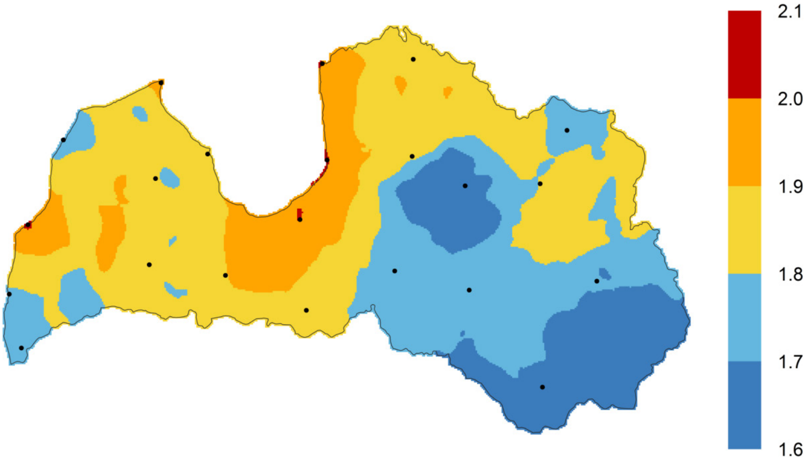

Fig. 6. Model of the spatial distribution values of the shape parameter *k* of Weibull wind speed probability density at the height of 10 *m* above the ground.

The parameters *c* and *k* presented in the form of contour maps allow estimating the frequency characteristics of the wind speed distribution for any point in the territory of Latvia at an altitude of 10 *m* above the ground using Eq. 5. This greatly simplifies the assessment of the amount of wind energy that can be produced when choosing the location for the SWTG installation.

The values obtained using Eq. (1), (2), (4) and the values of the parameters of the Weibull wind speed frequency distribution function calculated on the basis of measurements at the meteorological observation station in Ainazi, Daugavpils, Priekuli, Saldus and Ventspils for the measurement period from 1 January 2015 to 31 December 2016 are given in Table 2.

Table 2. The Values of Parameters *c* and *k* of the Weibull Wind Speed Frequency Distribution Function, Average Wind Speed V_{avg}, $V_{avg.cub}$ and Wind Energy Density in Relative Units $P'_{avg.i}$ for the Selected Meteorological Observation Stations

Stations	**Measurement results**					
	c	k	V_{avg}	$V_{avg.cub}$	$P'_{avg.i}$
Ainazi	4.3	2.0	3.8	4.7	0.66
Daugavpils	2.8	1.6	2.5	3.3	0.23
Priekuli	3.9	1.8	3.4	4.5	0.58
Saldus	3.4	1.8	3.0	3.9	0.38
Ventspils	4.6	1.7	4.1	5.4	1.00

The amount of power produced by a wind power converter in a certain period is determined as follows:

$$W(V) = \sum_{i=1}^{n} (P(V_i) \cdot F(V_i)) \ , \qquad (6)$$

where (V_i) – generator power curve value for wind speed V_i; $F(V_i)$ – Weibull frequency distribution function value for wind speeds V_i.

Weibull wind speed frequency distribution function *F(V)*, corresponding to the wind type observed in Ventspils region, is presented in Fig. 7 along with the power curve P(V) for *HAWT 2.5 kW*. In Fig. 7

the area, represented by Eq. 6, corresponds to the AEP of HAWT 2.5 *kW* in Ventspils region equal to W = 4.6 *MWh*. Functions $P(V)$ and $F(V)$ were used in the form of discrete bins with 1.0 *m/s* step length. Wind speed for the *i*-th step is determined as follows:

$$V_i = \Delta V \cdot i \ , \tag{7}$$

where ΔV – bin size 1 *m/s*; i – 1, 2…n.

The efficiency of WECS is characterised by the capacity factor C_e, which is defined as a ratio of the estimated value of W to the potential value of the energy produced by the generator W_r, assuming that it operates at the rated capacity during the entire period under consideration. Thus, in order to calculate the value of the capacity factor, the following expression is used:

$$C_e = \frac{W}{W_r} \cdot 100(\%) \, . \tag{8}$$

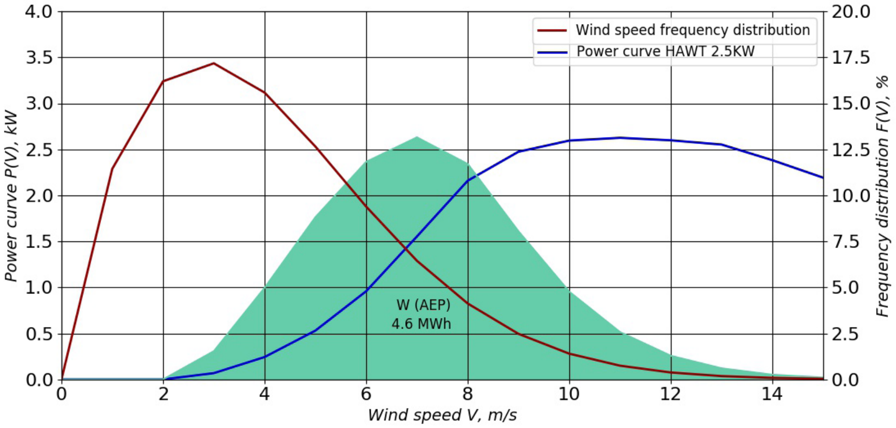

Fig. 7. Wind speed frequency distribution function F(V), the power curve P(V) for HAWT 2.5 *kW* and the value of AEP W = 4.6 *MWh*, corresponding to wind type at Ventspils meteorological observation station.

The results of the SWTG operational efficiency forecasts depending on the type of wind turbine, rated generator power and the location of its installation for the selected meteorological observation stations (Ainazi, Daugavpils, Priekuli, Saldus and Ventspils) are summarised in Table 3.

Table 3. Capacity Factor C_e, for HAWT and VAWT Type of the SWTG with Rated Power of 0.75, 2.5, 5.0, 20.0 *kW* and 0.75, 2.5, 6.0 *kW* at the Selected Meteorological Observation Stations

Stations	**Capacity factor C_e, %**						
	HAWT				**VAWT**		
	0.75 *kW*	**2.5 *kW***	**5.0 *kW***	**20.0 *kW***	**0.75 *kW***	**2.5 *kW***	**6.0 *kW***
Ainazi	9.89	16.77	11.27	5.94	4.56	3.07	3.41
Daugavpils	3.08	5,53	3.84	1.87	1.60	0.67	1.10
Priekuli	8.06	13.67	9.25	4.88	3.79	2,49	2.82
Saldus	5.08	8.91	6.11	3.02	2.46	1.24	1.76
Ventspils	13.33	21.24	14.56	8.49	6.45	5.24	4.96

The summary of the estimates of capacity factor C_e for generators of HAWT and VAWT type in Ventspils region are presented in Fig. 8. The comparison shows that regardless of the type, the efficiency of the wind turbine operation decreases with the increasing its rated power. The results of the study suggest that the generators of HAWT type, at the height of at least 10 *m* above the ground, are more suitable for operating in wind conditions of Latvia compared to VAWT type generators. Moreover, it is expected that among the wind energy converters of HAWT type considered in the study, generator with the rated power of 2.5 *kW* will tend to operate with the highest efficiency.

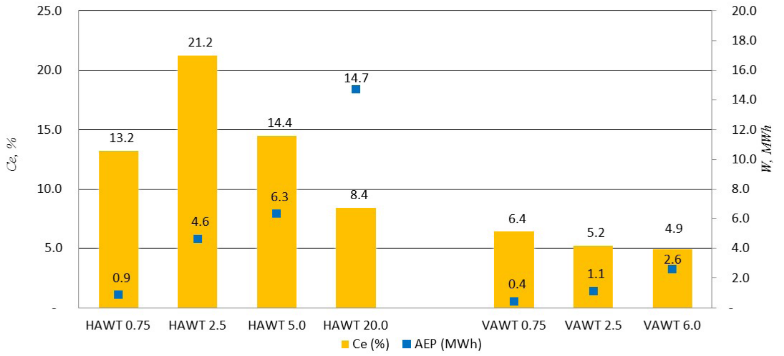

Fig. 8. Forecasted values of capacity factor C_e and AEP for HAWT generators with rated power of 0.75, 2.5, 5.0, 20.0 *kW* and VAWT Darrieus H-type 0.75, 2.5, 6.0 *kW* for Ventspils site.

The efficiency of WECS in the territory of Latvia can be represented as a model of the spatial distribution of the capacity factor C_e in relative units. Taking the maximum value of the capacity factor $C_{e\,max}$ to serve as the basis, the relative capacity factor C'_e for each meteorological observation station can be determined from Eq. 9:

$$C'_{e\,i} = {}^{C_{e\,i}}\!/_{C_{e\ \max}}\ , \qquad (9)$$

where $C_{e\ \max}$ – value of the capacity factor corresponding to the performance of HAWT 2.5 *kW* wind power converter for the type of wind observed at Ventspils station; $C_{e\,i}$ – value of the capacity factor corresponding to the efficiency of the HAWT 2.5 *kW* type generator for the wind type at each of the 22 stations.

In this case, the maximum value of the capacity factor corresponds to the SWTG of HAWT type with rated power of 2.5 *kW*, technical characteristics of which are summarised in Table 1, operating in the meteorological conditions observed at Ventspils observation station.

The developed model of the spatial distribution of factor in relative units is presented in the form of a color contour map in Fig. 9. The figure identifies areas within which HAWT 2.5 *kW* is expected to work with the certain level of efficiency relative to the one projected for Ventspils region. Thus, the results of the presented study can serve as a tool for estimating and forecasting the feasibility of the commercial use of small wind turbine generators at the altitude of 10 *m* in the territory of Latvia.

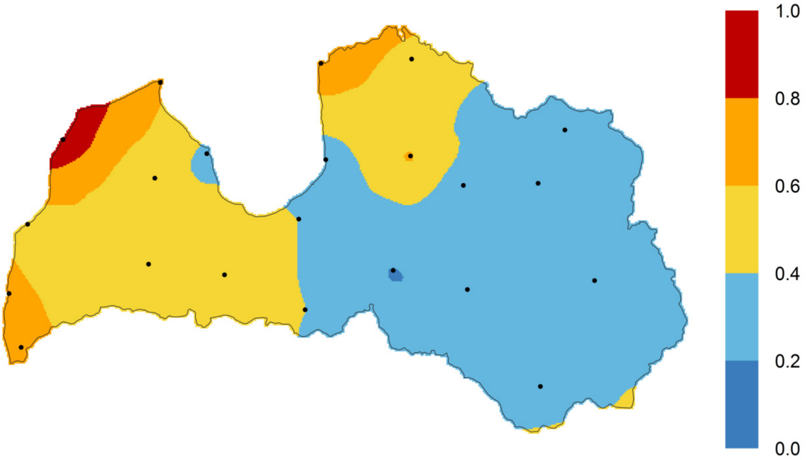

Fig. 9. Model of the spatial distribution of the relative capacity factor for HAWT type generator with rated power of 2.5 *kW* at the height of 10 *m* above the ground.

5. CONCLUSIONS

The national network of 22 meteorological stations in Latvia provides a unique opportunity for compiling the map of the spatial distribution of wind energy potential in the country at the height of 10 *m* above the ground.

The study presented the spatial distribution models of average wind speed, parameters of Weibull wind speed distribution, relative wind energy density and operational efficiency of the SWTG at the height of 10 *m* above the ground. The spatial models were presented in the form of colour contour maps.

The study provided the comparative analysis of two SWTG types: HAWT type with rated power of 0.75, 2.5, 5.0, 20.0 *kW* and VAWT Darrieus H-type with rated power of 0.75, 2.5, 6.0 *kW*. The results of the comparison suggest that HAWT type generators with rated power of 2.5 *kW* would tend to perform better than other WECS under consideration in terms of efficiency in Latvian meteorological conditions.

The results of the study can serve as a tool for forecasting AEP and estimating the feasibility of the commercial use of wind energy at the height of 10 *m* in the territory of Latvia.

ACKNOWLEDGEMENTS

The research has been carried out within the projects of the Ministry of Economics of the Republic of Latvia "Innovative Smart Grid Technologies and Their Optimization (INGRIDO)", project No. VPP-EM-INFRA-2018/1-0006 and "Future-Proof Development of the Latvian Power System in an Integrated Europe (FutureProof)", project No. VPP-EM-INFRA-2018/1-0005.

REFERENCES

1. Bezrukovs, D., & Sauhats, A. (2017). Economic and Operational Risks in Wind Energy Projects in Latvia. *Renewable Energy and Power Quality Journal*, *15*, 1–6. ISSN 2172-038X.: DOI:10.24084/repqj15.326.
2. Sauhats, A., Zemīte, L., Petričenko, Ļ., Moškins, I., & Jasevičs, A. (2018). Estimating the Economic Impacts of Net Metering Schemes for Residential PV Systems with Profiling of Power Demand, Generation, and Market Prices. *Energie*s, *11* (11), 1–19. DOI: 10.3390/en11113222.
3. Petrichenko, L., Broka, Z., Sauhats, A., & Bezrukovs, D. (2018). Cost-benefit analysis of Li-Ion batteries in a distribution network. In *Proceedings of the 2018 15th International Conference on the European Energy Market (EEM)*, 27–29 June 2018 (pp. 1–5). Łódź, Poland.
4. Zemite, L., Petrichenko, L., Sauhats, A., Linkevics, O., & Bockarjova, G. (2018). A Comparative Assessment of the Small-Scale Distributed Generation Policies in the EU and Latvia. In *Solar & Wind Integration Workshop: E-Mobility Integration Symposium*, *1/2018*, (pp. 1–6).
5. Shipkovs, P., Kashkarova, G., Lebedeva, K., & Migla, L. (2012). Use of renewable energy resources for reduction of environmental pollutions. *The Fourth IASTED African Conference on Power and Energy Systems* (AfricaPES 2012), (79–85), 3–5 September 2012, Gaborone, Botswana. CD Proceedings, ISBN: 978-0-88986-929-5.
6. Bobinaite, V., & Priedite, I. (2015). RES-E Support Policies in the Baltic States: Electricity Price Aspect (Part II). *Latvian Journal of Physics and Technical Sciences*, *2*, 13 – 25.
7. Ostapenko, J., & Gamalejevs, A. (2004). *Latvian wind energy guide*. Riga, 96 p. Available at http://www.windenergy.lv/startpage/lv/
8. Bezrukovs, V., Zacepins, A., Bezrukovs, V., & Komashilovs, V. (2016). Investigations of Wind Shear Distribution on the Baltic Shore of Latvia. *Latvian Journal of Physics and Technical Sciences*, *53* (3), 3–10.
9. Aniskevich, S., Bezrukovs, V., Zandovskis, U., & Bezrukovs, D. (2017). Modelling the spatial distribution of wind energy resources in Latvia. *Latvian Journal of Physics and Technical Sciences*, *54* (6), 10–20. DOI: 10.1515/lpts-2017-0037.
10. Bezrukovs, V., Bezrukovs, Vl., & Zacepins, A. (2014). Comparative Efficiency of Wind Turbines with Different Heights of Rotor Hubs: Performance Evaluation for Latvia. *J. Phys.: Conf. Ser. 524 012113.* DOI:10.1088/1742-6596/524/1/012113.
11. Godoy Simões, M., & Farret, F.A. (2014). *Modelling and analysis with induction generators* (3rd ed.). CRC Press.
12. Manwell, J. F., McGowan, J. G., & Rogers, A. L. (2009). *Wind energy explained: Theory, design and application*. USA: John Wiley & Sons Ltd.
13. Catalogue of European Urban Wind Turbine Manufacturers. (2017). Available at http://www.urbanwind.net/pdf/CATALOGUE_V2.pdf
14. Bezrukovs, V., Zacepins, A., Bezrukovs, Vl., & Komashilovs, V. (2016). Comparison of Methods for Evaluation of Wind Turbine Power Production by the Results of Wind Shear Measurements on the Baltic Shore of Latvia. *Renewable Energy*, *96*, Part A, 765–774.
15. Storch, H. von, & Zwiers, F.W. (2003). *Statistical analysis in climate research*. Cambridge: Cambridge University Press.
16. Ripley, B., Venables, B., Bates, D.M., Hornik, K., Gebhardt, A., Firth, D. (2017). *Support Functions and Datasets for Venables and Ripley's MASS*. Available at https://cran.r-project.org/web/packages/MASS/
17. Kharin, V.V., & Zwiers, F.W. (2000). Changes in the Extremes in an Ensemble of Transient Climate Simulations with a Coupled Atmosphere–Ocean GCM. *Journal of Climate*, *13*, 3760–3788.